

UNCLASSIFIED

Defense Technical Information Center
Compilation Part Notice

ADP012078

TITLE: Numerical Modeling of Supercavitating Flows

DISTRIBUTION: Approved for public release, distribution unlimited

This paper is part of the following report:

TITLE: Supercavitating Flows [les Ecoulements supercavitants]

To order the complete compilation report, use: ADA400728

The component part is provided here to allow users access to individually authored sections of proceedings, annals, symposia, etc. However, the component should be considered within the context of the overall compilation report and not as a stand-alone technical report.

The following component part numbers comprise the compilation report:
ADP012072 thru ADP012091

UNCLASSIFIED

Numerical Modeling of Supercavitating Flows

I.N. Kirschner, PhD • Neal E. Fine, PhD • James S. Uhlman, PhD • David C. Kring, PhD

Anteon/Engineering Technology Center
240 Oral School Road, Suite 105
Mystic, CT 06355
United States of America

SUMMARY

Supercavitating bodies can achieve very high speeds under water by virtue of reduced drag: with proper design, a cavitation bubble is generated at the nose and skin friction drag is drastically reduced. Depending on the type of supercavitating vehicle under consideration, the overall drag coefficient can be an order of magnitude less than that of a fully wetted vehicle. Slender-body theory and boundary element methods are two modern computational methods applied to the design of supercavitating vehicles. These course notes present recent advances in the theory behind these two computational approaches, as well as results and application of the methods to the simulation and control of supercavitating vehicles.

1 INTRODUCTION

Naval hydrodynamics and the marine engineering sciences have been characterized by centuries of evolutionary innovation punctuated by several revolutionary performance improvements. The relatively continuous improvement in early paddle wheel technology, for example, became obsolete very quickly upon introduction of the screw propeller in the late nineteenth century. The development of undersea vehicles has seen several similar paradigm shifts, such as the introduction of piston engines appropriately packaged to fit within a typical vehicle envelope, and the application of acoustical homing techniques. However, until recently, there has been little interest in very high speeds for undersea applications.

There are two primary impediments to increasing underwater vehicle speeds: current propulsion capability and the relatively high drag of current underwater vehicle configurations. For most of the last century in this country, relatively little research has been devoted to significantly opening the performance envelope in these areas. Over the last decade, however, high-speed capability has received increased attention, and dramatic advancements have been made. These achievements have been supplemented with information concerning international development (LEGI, 2000).

The history of hydrodynamics research displays an emphasis on eliminating cavitation, chiefly because of the erosion, vibration, and acoustical signatures that often accompany the effect. The drag-reducing benefits of cavitation, however, were noted during the first half of the last century, and have received significant attention over the last decade.

Supercavitation is a hydrodynamic process by which a submerged body is almost entirely enveloped in a layer of gas. Because the density and viscosity of the gas is dramatically lower than that of seawater, skin friction drag can be reduced dramatically. If the body is shaped properly, the attendant pressure drag can be maintained at a very low value, so that the overall body drag is also reduced significantly. The process of designing a supercavitating body for minimum pressure drag, while addressing issues of control and maneuvering, is greatly aided by the use of modern computational methods.

This document presents details of two computational methods that have been applied extensively during the past decade to the analysis and design of supercavitating bodies: boundary element methods and slender-body theory. Section 2 lays the groundwork with a discussion of several issues pertinent to the numerical modeling, including a motivation for the application of

potential flow techniques to prediction of supercavitating flows. Section 3 presents results from several applications of boundary element methods, including steady axisymmetric flows, unsteady flows, and cavitating fins. Section 4 contains a discussion of slender-body theory and some pertinent results. In section 5, we present the results of numerical flight simulation for supercavitating vehicles that incorporates some of the computational methods discussed in previous sections in determining the forces experienced by the vehicle in maneuvers.

These lecture notes were derived from several previous publications. The nomenclature schemes of the original publications have been retained, but each sub-section is reasonably self-consistent.

2 PRELIMINARY REMARKS

2.1 Vehicle Control

A properly shaped supercavitating body will have a very small pressure drag, so that the overall body drag is also reduced dramatically over that of a fully wetted body. However, because the center of pressure is typically located well forward with respect to the center of gravity, control and maneuvering present special challenges. Also, whereas a fully wetted vehicle develops substantial lift in a turn due to vortex shedding off the hull, a supercavitating vehicle does not develop significant lift over the gas-enveloped surfaces. This requires a different approach to effecting hydrodynamic control, and increases the relative advantage of a banked maneuvering strategy.

A supercavity can be maintained in one of two ways: (1) by achieving such a high speed that the water vaporizes near the nose of the body, generating a cavity that grows to exceed the length of the body; or, (2) by supplying gas to the cavity at nearly ambient pressure at more moderate (but still very high) speeds. The first technique is known as vaporous cavitation; the second is termed ventilation, or artificial cavitation. Schematic views of two types of notional supercavitating bodies are shown in Figure 1. Note that each concept involves a cavitator (in this case a disk) with a salient edge that ensures clean cavity formation near the nose of the body. The relatively small diameter of the cavitator with respect to that of the vehicle is also important: it is this feature that allows the pressure drag to be maintained at a manageable level. An important step in the design of a supercavitating body is selection of a cavitator that is appropriately sized for the vehicle and speed of interest.

Control of supercavitating vehicles presents special challenges not normally associated with fully wetted vehicle dynamics. These arise from the absence of certain physical effects such as lift on the body and from the presence of other effects such as the nonlinear interaction of the control surfaces and the body with the cavity wall.

In contrast with the controlled vehicle depicted in Figure 1b, a projectile of the type shown in Figure 1a need not have fins, since the global stability of the trajectory is maintained via occasional tail-slap contact of the afterbody with the cavity boundary (or, at extremely high speeds, by the forces due to the relative motion between the vapor and the body). Since the vehicle shown in Figure 1b would incorporate some sort of guidance system, fins have been indicated that would provide hydrodynamic control in concert with actuation of the cavitator. The blast tube (that is, the small-diameter section of the vehicle aft of the fins) shown in Figure 1b is expected to represent a more optimal shape than a cylinder of constant radius for certain classes of supercavitating vehicles: if range is critical, then drag must be minimized, which (in turn) entails minimization of the cavity diameter. The step at the after end of the mid-body allows for this.

2.2 Drag Components for Submerged Bodies

For simplicity, consider an undersea vehicle with constant mass. This excludes rocket propulsion, but is illustrative of the physics of supercavitation drag reduction. The following analysis of the drag force is equally applicable to rocket-propelled vehicles; however, the basic equation of vehicle motion (equation 2.1) must be modified to account for the ejection of mass (Greenwood, 1965).

Newton's second law of motion applied to undersea vehicles can be written (Greenwood, 1965) as

$$T - D = \frac{d}{dt}(mU) \quad (2.1)$$

where m is the vehicle mass plus the hydrodynamic added mass (Newman, 1980) and U is the velocity of the vehicle in straight and level flight along a trajectory parallel to the thrust vector. Under steady conditions, the thrust provided by the propulsion system, T , balances the vehicle drag, D . For this simple case, the dynamics and hydrodynamics of the vehicle are usually analyzed in a body-fixed frame of reference, as shown in Figure 2.

The drag represents an integration over the vehicle surface of all components of stress acting opposite to the direction of travel (Newman, 1980):

$$D = \oint_S (pn_x + n_y \tau_{yx} + n_z \tau_{zx}) dS \quad (2.2)$$

where p is the pressure, τ_{yx} and τ_{zx} are the components of the shear stress in the x -direction, and $n = (n_x, n_y, n_z)$ is the unit vector normal to the surface of the vehicle.

It is often convenient to separate the total drag force into components representing the pressure and skin-friction contributions:

$D = D_p + D_f$ where D_p is the pressure drag and D_f is the skin-friction drag.

It should be noted that, for vehicles traveling close to a free surface, generation of gravity and capillary waves is associated with a modification of the pressure and velocity fields on the vehicle hull, causing a drag increase. Also, at speeds greater than the lower critical Mach number, there is a drag increase associated with the shock wave system (Ashley and Landahl, 1965). In most cases of interest, the primary drag component affected is the pressure drag. For purposes of analysis, each contribution is often treated as a separate component, although some coupling of the terms occurs. Free-surface drag will not be considered in the following discussion. A compressible flow formulation using slender-body theory is presented in a later section, but discussion of the associated effects on drag is relegated to the originating publication, Varghese, et al, (1997).

Denoting the fluid density as ρ and the free stream speed as U_∞ , the drag is typically normalized on the product of the dynamic pressure of the free stream, $\frac{1}{2}\rho U_\infty^2$, and a characteristic area, A . For axisymmetric undersea vehicles, A is usually chosen as the maximum sectional area. Thus,

$$C_D = \frac{D}{\frac{1}{2}\rho U_\infty^2 A} \quad (2.3)$$

2.3 Governing Equations

Neglecting the effect of gravity (assuming that free-surface and stratification effects are unimportant for the case under consideration), the equations of motion of a fluid in a volume V in the incompressible limit describe conservation of mass:

$$\nabla \cdot \mathbf{U} \equiv 0 \quad (2.4)$$

and conservation of momentum:

$$\left[\frac{\partial}{\partial t} + (\mathbf{U} \cdot \nabla) \right] \mathbf{U} = -\frac{\nabla p}{\rho} + \nu \nabla^2 \mathbf{U}, \quad (2.5)$$

where ν is the fluid kinematic viscosity. The momentum conservation equations are referred to as the Navier-Stokes equations.

The relative importance of the terms on the right-hand side of equation 2.6 can be gleaned by making the entire system dimensionless, as follows:

$$\tilde{U} = \frac{\Delta U}{U_\infty} \quad \tilde{t} = \frac{\Delta U_\infty t}{L} \quad \tilde{\nabla} = L \nabla$$

where L is some length characterizing the flow. For axisymmetric undersea vehicles, this length is usually chosen as the maximum diameter. Making these substitutions into equations 2.5 and 2.6, rearranging, and dropping the tildes gives

$$\nabla \cdot \mathbf{U} \equiv 0 \quad (2.6)$$

$$\left[\frac{\partial}{\partial t} + (\mathbf{U} \cdot \nabla) \right] \mathbf{U} = -\frac{L}{2} \nabla C_p + \frac{1}{R} \nabla^2 \mathbf{U}, \quad (2.7)$$

where

$$C_p = \frac{\Delta p - p_\infty}{\frac{1}{2} \rho U_\infty^2} = \text{pressure coefficient} \quad (2.8)$$

and

$$R = \frac{\Delta U_\infty L}{\nu} = \text{Reynolds number}. \quad (2.9)$$

Prandtl noted that, as the Reynolds number increases, viscous effects become increasingly confined to a thin boundary layer near the body surface (Schlichting, 1979). This fact, in conjunction with certain mathematically provable laws of fluid motion (Yih, 1979), allows use of potential flow techniques in predicting the motion of high-Reynolds-number flows past bodies (Newman, 1980). Under these conditions, the velocity field can be determined based solely on kinematic considerations and knowledge of conditions at the boundaries of the fluid. Once the irrotational velocity field is known, an auxiliary equation for pressure is given by a simple form of Bernoulli's equation (Aris, 1962):

$$p + \frac{1}{2} \rho U^2 = p_\infty + \frac{1}{2} \rho U_\infty^2. \quad (2.10)$$

The far field pressure, p_∞ , is simply the hydrostatic pressure at the operating depth of the vehicle.

When the pressure of a liquid is reduced below some threshold level at constant temperature it vaporizes. This change of phase is known as cavitation (Newman, 1980). The threshold value for a pure liquid undergoing quasi-static pressure reduction is known as the vapor pressure, p_v . Cavitation inception is often enhanced in the field due to various perturbations of ideal conditions, including the amount of gases absorbed in the liquid, contamination by other liquids or solids, or the presence of bubbles. The vapor pressure provides an excellent measure of the cavitation inception pressure under most conditions of interest, however.

As fluid flows past a fully wetted body, the pressure increases to stagnation pressure at the forward stagnation point, decreases below ambient pressure, then increases toward stagnation pressure over the afterbody. The actual pressure recovery depends on the development of the boundary layer and the extent of separation.

If the pressure falls below the fluid vapor pressure at any point, a vapor cavity will form. The density of the vapor within the cavity is orders of magnitude less than that of the ambient liquid. The dimensionless quantity characterizing the tendency of a given flow to cavitate is known as the cavitation number:

$$\sigma = \frac{\Delta p_\infty - p_c}{\frac{1}{2} \rho U_\infty^2} \quad (2.11)$$

where p_c is the cavity pressure. For non-ventilated flows, the cavity pressure is approximately equal to the vapor pressure of the ambient liquid under most conditions of current interest.

As the velocity increases, the cavitation number and the minimum pressure on the body surface decrease, and the fluid tends to cavitate. Below a certain cavitation number, an experimentally observed fact (one that may be explained by considering the various terms in the momentum equation, equation 2.5) is that the velocity within the vapor cavity is very small. Consequently, to lowest order, the pressure within the vapor cavity is constant, with a value nearly equal to the vapor pressure of the fluid. At high Reynolds number, the shear layer forming the cavity boundary is thin. In that case, potential flow techniques may be used to predict such flows (Newman, 1980). It should be noted that recent results of high-Mach-number research indicate that the assumption of negligible velocities within the cavity is not valid at very high speeds (say, at Mach numbers approaching unity). However, for cavity-riding vehicles, the pressure can be taken as constant within the vapor cavity.

In terms of velocity, the boundary-value problem describing the ideal supercavitating flow shown in Figure 3 is given by the field equation describing conservation of mass (equation 2.4) along with boundary conditions on velocity:

$$\mathbf{U} \cdot \mathbf{n} \equiv 0 \quad \text{on } S_w \cup S_c \quad (2.12)$$

$$\mathbf{U} \cdot \mathbf{s} \equiv U_\infty \sqrt{1 + \sigma} \quad \text{on } S_c \quad (2.13)$$

where S_w is the wetted surface of the body and S_c is the cavity boundary.

The dynamic condition results from applying Bernoulli's equation (equation 2.10) along the cavity streamline, under the constraint that the pressure within the cavity is constant with a value equal to the cavity pressure, p_c . Various techniques exist for solving such a problem, including panel methods and slender-body theory (Kuethe and Chow, 1976). These two approaches will be discussed in the following sections.

3 APPLICATION OF THE BOUNDARY-ELEMENT METHOD

This section describes application of the boundary element method to prediction of supercavitating flows. Three sample problems are discussed: (1) steady, subsonic flow around an axisymmetric disk; (2) unsteady, subsonic flow around general cavitator shapes; and (3) steady flow around cavitating control effector fins for application to supercavitating vehicle flight control.

3.1 Steady Axisymmetric Flows

This sub-section is derived from Kirschner, et al, (1995).

The physical problem is shown in the schematic drawing of Figure 4. The body is axisymmetric and oriented parallel to the flow. The geometries under consideration in these lecture notes include only those for which a salient cavity detachment point can be identified, although the solution techniques described could be extended to more general shapes.

The position vector in a meridional plane is denoted as $\mathbf{x} = x\mathbf{i} + r\mathbf{j}$. The inner boundary of the flow problem is the union of the wetted portion of the body and the boundary of the cavity:

$$S = S_B \cup S_C \quad (3.1)$$

The lengths of the body and cavity are denoted as ℓ_B and ℓ_C , respectively. The total length of the combined body-cavity system is denoted as ℓ .

Only steady flows are considered in this sub-section. The difficulties of representing cavity closure under this assumption are discussed below.

Unit vectors normal and tangent to the body-cavity surface in a meridional plane are denoted as $\mathbf{n} = n_x\mathbf{i} + n_r\mathbf{j}$ and $\mathbf{s} = s_x\mathbf{i} + s_r\mathbf{j}$, respectively. The unit normal vector is directed into the liquid; the unit tangent vector is directed positive aft. $\mathbf{U}_\infty = U_\infty\mathbf{i}$ is the free stream velocity. The total velocity at any point outside of the body-cavity surface is decomposed as

$$\mathbf{U} = U_\infty\mathbf{i} + \mathbf{u} \quad (3.2)$$

where $\mathbf{u}(\mathbf{x}) = u_x \mathbf{i} + u_r \mathbf{j}$ is the disturbance velocity. As discussed above, to lowest order the cavity pressure, p_c

Potential Flow Formulation

The fluid is assumed to be incompressible and the flow is taken to be irrotational. The last assumption guarantees the existence of a velocity potential. Under this condition, the flow field is governed by Laplace's equation,

$$\nabla^2 \Phi = \Phi_{xx} + \Phi_{rr} + \frac{\Phi_r}{r} = 0, \quad (3.3)$$

where Φ is the total potential.

A disturbance potential, ϕ , can be defined from the total potential by

$$\Phi = U_\infty \cdot \mathbf{x} + \phi, \quad (3.4)$$

so that the disturbance velocity, \mathbf{u} , is given by the gradient of the disturbance potential. The disturbance potential also obeys the Laplace equation. This boundary value problem is shown in the schematic drawing of Figure 5.

Kinematic Condition

The requirement that the flow be tangential to the body and cavity surfaces, equation 2.12, combined with the definition of the potential in equation 3.4, gives the following kinematic condition on the body-cavity surface, S :

$$\frac{\partial \phi}{\partial n} = -\mathbf{n} \cdot \mathbf{U}_\infty \text{ on } S \quad (3.5)$$

Dynamic Condition On The Cavity

Bernoulli's equation applied along the cavity surface can be expressed as follows:

$$C_p = -\sigma \text{ on } S_C \quad (3.6)$$

The magnitude of the total velocity on the cavity surface is given by equation 2.13. From this, the following expression for the disturbance potential may be applied on the cavity surface:

$$\frac{\partial \phi}{\partial s} = U_\infty \sqrt{1 + \sigma} - U_\infty s_x \text{ on } S_C \quad (3.7)$$

Cavity Termination

For a given wetted body shape and cavity length, Laplace's equation for the disturbance potential can be solved subject to the kinematic condition, equation 3.5, and the dynamic condition, equation 3.7. A cavity termination model is also required.

In this work, a modified Riabouchinsky cavity termination model is used. The cavity is closed with a Riabouchinsky wall or endplate extending from the axis of symmetry to the point at which the cavity streamline becomes perpendicular to the axis. Along the endplate, denoted as S_W , the kinematic condition is satisfied. In the current case, since the flow is axisymmetric, the endplate is always perpendicular to the axis of symmetry.

It should be noted that this termination model has been chosen as a compromise between simplicity and physical validity. The reentrant jet model is a closer representation of the physical flow, but is more difficult to implement numerically. The reentrant jet model is discussed in further detail below.

Solution Procedure using Boundary Elements

The disturbance velocity potential in equation 3.4 satisfies Green's third identity, a Fredholm integral equation of the second kind, along the body, cavity, and endplate (Lamb, 1945). Thus, for

any field point \mathbf{x} on the body-cavity surface, the disturbance velocity potential can be computed from

$$2\pi\phi(\mathbf{x}) = -\oint\oint \left[\phi(\mathbf{x}') \frac{\partial}{\partial n} G(\mathbf{x}; \mathbf{x}') - \frac{\partial}{\partial n} \phi(\mathbf{x}') G(\mathbf{x}; \mathbf{x}') \right] dS(\mathbf{x}') \quad (3.8)$$

where the integration is performed over source points, \mathbf{x}' , along the entire body, cavity, and endplate surface. Green's function for this problem, $G(\mathbf{x}; \mathbf{x}')$, is

$$G(\mathbf{x}; \mathbf{x}') = \frac{1}{|\mathbf{x} - \mathbf{x}'|} \quad (3.9)$$

Along the body and the endplate surfaces, the source strength distribution, $\partial\phi/\partial n$, is known and given by equation 3.5. Along the cavity surface, an expression for the dipole strength distribution, ϕ , can be found by integrating equation 3.7:

$$\phi(s) = \phi(s_0) + U_\infty \sqrt{1+\sigma} (s - s_0) - U_\infty (x - x_0) \text{ on } S_C. \quad (3.10)$$

where s_0 is the arc length coordinate at an arbitrary fixed point on the body-cavity surface, S .

To solve for the dipole strength distribution, ϕ , along the body and endplate surfaces, and the source strength distribution, $\partial\phi/\partial n$, along the cavity boundary, the computational domain is discretized into M_B panels along the body, M_C panels along the cavity, and M_W panels along the endplate. Unequal spacing of the panels is utilized to ensure that more panels are concentrated where large velocity gradients are expected.

The source and dipole strengths are taken to be constant on each panel. Integral equation 3.8 is satisfied at control points on every panel. These are chosen such that each trapezoidal panel is divided into equal areas upstream and downstream of its control point.

The unknowns to be determined are therefore

- M_B dipole strengths on the body panels;
- M_C source strengths on the cavity panels;
- M_W dipole strengths on the endplate panels; and,
- the dimensionless cavity surface velocity, $\sqrt{1+\sigma}$.

There are $M_B + M_C + M_W + 1$ quantities to be determined. Equation 3.8 gives $M_B + M_C + M_W$ equations. The zero net flux condition,

$$\oint_S \frac{\partial\phi}{\partial n} dS = 0 \quad (3.11)$$

is used as another condition to form a determinate system.

Cavity Shape For Fixed Cavity Length

For the body shapes considered in these lecture notes, the cavity detachment point is known. For a specified cavity length, a cavity profile is assumed, and the potential-based boundary element method used to solve for the dimensionless cavity surface velocity, $\sqrt{1+\sigma}$, and the source and dipole strengths. A new estimate of the cavity profile is then determined by applying the kinematic condition on the cavity surface, S_C . The boundary value problem is then re-solved, and the process repeated until the cavity profile converges.

The kinematic condition, equation 3.5, can be written as

$$n_x (u_x + U_\infty) = -n_r u_r. \quad (3.12)$$

For example, if the body cavity surface profile is defined by $y = b(x)$, then

$$\frac{db}{dx} = -\frac{n_x}{n_r} = \frac{u_r}{u_x + U_\infty} \quad (3.13)$$

along the cavity surface.

Prior to convergence of the cavity profile, the kinematic condition on the cavity boundary has not been imposed. Thus, the object is to change the cavity shape such that the flux across the boundary is minimized. Two methods have been tested for modifying the cavity shape including (1) modification of the profile offset; and, (2) sequential modification of each panel angle followed by re-scaling of the cavity to its original length. In practice, the latter approach has proven to be more general and robust than the former.

Pressure and Drag

Once the potential flow problem outlined in the previous section has been solved, the pressure coefficient on the body surface, S_B , can be computed as

$$C_p = 1 - \left(\frac{U_s}{U_\infty} \right)^2 = 1 - \left(s_x + \frac{1}{U_\infty} \frac{\partial \phi}{\partial s} \right)^2 \quad (3.14)$$

The body drag is the integral of the x -component of the differential pressure force over the wetted portion of the body and the base:

$$D = - \left[\iint_{S_B} p n_x \, dS + \pi B^2 p_C \right] \quad (3.15)$$

Where B is the radius of the cavitator at the cavity detachment point. The drag coefficient is computed as:

$$C_D = \sigma - \frac{1}{\pi B^2} \iint_{S_B} n_x C_p \, dS \quad (3.16)$$

Selected Results – Steady Flows

Sample results of the fully axisymmetric boundary element method for incompressible flow are presented in Figure 6 through Figure 8. For additional results and discussion, refer to Kirschner, et al, (1995).

The body-cavity profiles predicted for a 15° cone at several cavitation numbers are shown in Figure 6. The predicted drag coefficients at each cavitation number are plotted in Figure 7 and compared with the empirical curve fit of May (1975):

$$C_D = 0.151 + 0.587\sigma \quad (3.17)$$

It can be seen that the trend is very accurate. Since the publication of Kirschner, et al (1995), a coding error was discovered which, when corrected, virtually eliminated the offset seen in Figure 7.

The predicted maximum cavity diameter is compared with the empirical curve fit of May (1975) in Figure 8. The following equation represents the curve fit:

$$\frac{1}{C_D} \left(\frac{b_{\max}}{B} \right)^2 \cong 1.28\sigma^{-0.91} \quad (3.18)$$

The left-hand side of equation 3.18 is the function plotted on the ordinate of Figure 8. The prediction appears to be excellent. Note from the figures that, if the predicted drag coefficient used in equation 3.18 is replaced with that given by equation 3.17, the prediction of values characterizing the cavity geometry is improved. It should be noted that May's equation over-predicts experimental cavity lengths at higher cavitation numbers.

Reentrant Jet Termination Model

A termination model that better represents the physics for typical supercavitating flows of interest is the reentrant jet model, a description of which may be found in Tulin (1964). The current formulation is based on Uhlman, et al, (1998).

For axisymmetric flows, the presence of the reentrant jet may be handled quite simply by truncating an axisymmetric reentrant surface at a jet face, and assuming that, at this axial location, this surface is asymptotic to a cylinder of constant diameter and the cavity surface velocity has approached a constant limit. In the absence of gravity, and assuming that the truncated jet face is perpendicular to the velocity, the conditions at the jet face are

$$\frac{\partial \Phi}{\partial n} = U_{\infty} \sqrt{1 + \sigma} \quad (3.20)$$

and

$$\frac{\partial \Phi}{\partial s} = 0. \quad (3.21)$$

With the disturbance potential defined by equation 3.4, the conditions to be applied at the jet face become

$$\frac{\partial \phi}{\partial n} = U_{\infty} (\sqrt{1 + \sigma} + 1) \quad (3.22)$$

and

$$\frac{\partial \phi}{\partial s} = 0. \quad (3.23)$$

Note that for two-dimensional reentrant jets with lift the conditions are more complicated. Figure 9 shows a sample computed cavity shape for a two-dimensional flat plate cavitator at an angle of attack.

3.2 General Incompressible Flows

This section, which is based on Kring et al (2000), presents some initial results for a fully three-dimensional time-domain simulation of the flow about general supercavitating bodies. The intent of the effort is to study various ventilated cavitators, lifting appendages, and bodies that may penetrate the cavity wall. The time-domain approach, useful for the formulation of the nonlinear boundary conditions on the cavity free surface, will also allow the application of this method to flight simulation and control studies (see section 5).

In this fully three-dimensional initial value problem for a moving, cavitating body, several boundary conditions must be specified. These include the body boundary condition, nonlinear cavity conditions on the moving free surface, a reentrant jet closure, and a shed wake sheet. At each time step, these conditions are integrated both in time and in space and combined with the governing Laplace equation to produce a boundary value problem that is formulated as a boundary integral equation of the mixed Neumann-Dirichlet type.

The numerical scheme in this paper has been adapted from a boundary-element method developed for free-surface gravity waves interacting with submerged and floating bodies (Kring, et al, 1999), with guidance for the cavity boundary and jet closure conditions from Uhlman (1987 and 1989) and Fine and Kinns (1993). The free surface scheme was designed in accordance with the numerical stability analysis of Vada and Nakos (1993). A key result of that analysis was the demonstration that both high-order elements and mixed explicit-implicit time marching are needed for numerical stability. The boundary-element method employed here is a high-order, B-spline-based approach developed originally by Maniar (1995) with a so-called fast or accelerated solver

developed by Phillips and White (1997) and applied in Kring, et al, (1999b). Whereas direct solution of full matrices requires computational effort proportional to the cube of the number of unknowns, N , -- that is, effort of order N^3 , or $O(N^3)$ -- and other traditional methods may show improved performance of $O(N^2)$, the accelerated method discussed in this section is $O(N)$.

Figure 10 illustrates the potential flow, initial boundary-value problem for a cavitating disk with a trailing cavity, reentrant jet closure, and shed wake. The body may have any shape and the method may be extended to add lifting appendages and planing bodies.

In order to provide a computational window to track this moving body, the three-dimensional problem is defined with respect to a mean-body frame of reference, \bar{x} . Points in the inertial frame, \bar{x}_I , are related to the mean-body frame by the relation:

$$\bar{x}_I = \bar{x} + \int_{t_0}^t \bar{U}(\bar{x}, \tau) d\tau, \quad (3.24)$$

where t is time. The motion of the mean-body frame, $\bar{U}(\bar{x}, t)$, is a function of space since it may be rotating with respect to the inertial frame, so that

$$\bar{U}(\bar{x}, t) = \bar{U}(0, t) + \bar{\Omega}(t)\bar{x}, \quad (3.25)$$

where $\bar{\Omega}(t)$ is a rotational transformation matrix and $\bar{U}(0, t)$ is the translation at the origin. The mean-body frame is defined about the assumed mean position of the disk cavitator, so that the disk tends to oscillate around $x = 0$.

Initial Conditions

The problem is started impulsively from an assumed initial geometry and distribution of potential. Two initial conditions have been considered. In the first case, the potential on the cavity is set to zero on an assumed surface. Physically, this can be considered as an artificial pressure and cavity location that is released at $t = 0$. If the cavitator disk is set in steady motion, the transients due to this artificial start-up should eventually decay. The second case involves solution of a Neumann problem in which the cavity is considered to be a fixed wall. The potential from this solution is then used as the initial condition for the time-domain simulation. The intent is to reduce the size of the startup transient.

Governing Equation

The potential flow exterior to the surface S (the union of the cavity S_{C^+} and S_{C^-} ; the body, S_B ; and the jet, S_J) is governed by the Laplace equation with allowance for the wake cuts collapsed onto the surface S_W . Hence,

$$\nabla^2 \phi = 0 \quad (3.26)$$

where ϕ is the disturbance potential.

Green's third identity, equation 3.8, is applied in a manner similar to that described for steady axisymmetric flows. In this case, however, we explicitly include an integration over the wake surface, S_W , as follows:

$$2\pi\phi(\bar{x}) + \iint_S (\phi(\bar{x}')G(\bar{x}; \bar{x}') - \phi_n(\bar{x}')G_n(\bar{x}; \bar{x}')) d\bar{x}' + \iint_{S_W} \Delta\phi(\bar{x}')G_n(\bar{x}; \bar{x}') d\bar{x}' = 0 \quad (3.27)$$

where the Green's function is defined by equation 3.9.

Cavity Conditions

The cavity conditions on S_{C^+} and S_{C^-} are posed in the curvilinear frame of reference defined by the parametric surface, $\vec{\xi}(u, v, t)$. The parametric coordinates, (u, v) , are the presumed streamwise and circumferential directions, respectively. This semi-Eulerian formulation is important for a numerically consistent representation of the boundary condition on the moving surface. Surface potentials, $\phi(u, v, t)$ and $\phi_0(v, t)$, are defined through the decomposition of the perturbation potential:

$$\phi(\vec{\xi}(u, v, t), t) = \phi(u, v, t) + \phi_0(v, t) \quad (3.28)$$

The first part of the surface potential, ϕ , satisfies the dynamic cavity condition implicitly in the numerical scheme. The second part, ϕ_0 , which is constant along the presumed streamline direction, u , satisfies continuity of the disturbance potential at the cavity detachment locus and appears explicitly in the dynamic cavity condition on the leading cavity surface.

Applying the chain rule to the decomposition leads to relations for the time-derivative and gradient:

$$\frac{\partial \phi}{\partial t} = \frac{\partial (\phi + \phi_0)}{\partial t} - \nabla_u (\phi + \phi_0) \cdot \nabla_u \vec{\xi} \quad (3.29)$$

and

$$\nabla \phi = \nabla_u (\phi + \phi_0) + \frac{\partial \phi}{\partial n} \hat{n} \quad (3.30)$$

where \hat{n} is the unit vector normal to the surface and ∇_u is the surface gradient operator defined by

$$\nabla_u f = \frac{\frac{\partial f}{\partial u} [\hat{u} - (\hat{u} \cdot \hat{v}) \hat{v}] + \frac{\partial f}{\partial v} [\hat{v} - (\hat{u} \cdot \hat{v}) \hat{u}]}{\|\hat{u} \times \hat{v}\|^2} \quad (3.31)$$

Here \hat{u} and \hat{v} are unit vectors that are non-orthogonal in general.

Kinematic Boundary Condition

The total time derivative of the function that defines the cavity surface must vanish. Applying the Gallilean transform from the inertial to the mean-body frame and defining the normal coordinate, n , and the surface displacement in the normal direction, $h(u, v, t) = \vec{\xi}(u, v, t) \cdot \hat{n}(u, v, t)$, yields the kinematic condition:

$$\frac{\partial h}{\partial t} - \vec{U} \cdot \nabla_u h = -\nabla_u (\phi + \phi_0) \cdot \nabla_u h - \vec{U} \cdot \hat{n} + \frac{\partial \phi}{\partial n} \quad (3.32)$$

Dynamic Boundary Condition

The dynamic condition specifies a constant pressure on the cavity surface at all times. The derivation of this condition begins with the unsteady Bernoulli condition in the inertial frame (referencing atmospheric pressure as zero). With $z = 0$ representing the mean ocean surface:

$$p_c = -\rho \left(\frac{\partial \phi}{\partial t} + \frac{1}{2} \nabla \phi \cdot \nabla \phi + gz \right) \quad (3.33)$$

where p_c is the cavity pressure.

Applying the Gallilean transform from the inertial to the mean-body frame and substituting relations for the surface potential yields

$$\frac{\partial \phi}{\partial t} - \vec{U} \cdot \nabla_u \phi = -\frac{\partial \phi_0}{\partial t} + \vec{U} \cdot \nabla_u \phi_0 + \left[(\vec{U} \cdot \hat{n}) \frac{\partial \phi}{\partial n} - \frac{1}{2} \nabla \phi \cdot \nabla \phi \right] - gz - \frac{p_c}{\rho} \quad (3.34)$$

Cavitator Wetted-Surface Condition

A Neumann body-boundary condition similar to equation 3.5 is applied to the cavitator wetted surface, S_B .

Jet Condition

The reentrant jet is artificially truncated (cut perpendicular to the streamline) and assumed to have reached a steady diameter with no cross-flow components and a pressure equal to the cavity pressure across the face of the cut. Thus, it has an imposed flux and an imposed pressure. Although this is intended to be a time-accurate formulation for the cavity problem, a steady-state jet condition has been used to date.

We start with the steady, dynamic boundary condition: equation 3.34 with the time derivative set to zero. If there is no cross-flow, then $\nabla \phi = \phi_n \hat{n}$ on the jet. Therefore, the jet condition becomes

$$U_n \frac{\partial \phi}{\partial n} - \frac{1}{2} \left(\frac{\partial \phi}{\partial n} \right)^2 = gz + \frac{p_c}{\rho}, \quad (3.35)$$

where $U_n = \vec{U} \cdot \hat{n}$.

Choosing the positive root, consistent with the cavity conditions, the jet flux then becomes:

$$\frac{\partial \phi}{\partial n} = U_n + \sqrt{U_n^2 - 2 \left(gz + \frac{p_c}{\rho} \right)} \quad (3.36)$$

With no cross-flow, the potential across the jet face must be constant at a given depth and is set equal to the potential on the adjacent cavity.

Cavity Detachment and Kutta Conditions

The additional potential, ϕ_0 , on the leading cavity surface, S_{C+} , that detaches from the cavitator body boundary is specified by a detachment condition across the body-cavity intersection, $\vec{x}|_{BE}$. With the further constraint that the first surface potential vanishes at the cavity detachment line, $\phi(u|_{BE}, v, t) = 0$, the additional potential is,

$$\phi_0(v, t) = \phi(\vec{x}|_{BE}, t), \quad (3.37)$$

which represents the cavity detachment condition. A cavity trailing edge is defined at the junction of the leading and lagging cavity surfaces where the potential jump across the wake is specified as

$$\Delta \phi|_{TE}(v, t) = (\phi^+|_{TE} - \phi^-|_{TE}) + \phi_0, \quad (3.38)$$

which comprises the Kutta condition. For a time-dependent wake, a nonlinear evolution equation should govern the propagation of the shed vorticity downstream, but, to date, a simplifying assumption has been used: The wake position is fixed and a steady state asymptotic distribution is assumed for the shed vorticity.

Numerical Implementation

The scheme begins with initial conditions for the geometry and the surface potential, ϕ , at time $t = 0$. The detachment conditions, the Kutta conditions, and the mixed boundary-integral equation are then solved simultaneously to find the normal velocity on the cavity surface and the potential on the body. This is referred to as the mixed BVP, which will be solved at each time step as the surface evolves. The cavity conditions and the mixed BVP must be integrated in time and space.

After the impulsive start, each step in the temporal integration begins by first satisfying the kinematic and dynamic boundary conditions to update the geometry and surface potential on the cavity. The mixed BVP is then solved to update the potential on the body and the normal velocity on the cavity.

To summarize, at the start-up ($t = 0^+$):

0. Given initial conditions ϕ^0, ξ^0 on S_C solve mixed BVP for ϕ_n^0 on S_C .

At each subsequent time-step:

1. Determine body motion: impose or solve equation of motion.
2. Integrate the kinematic condition on the cavity to find ξ^{n+1} on S_C .
3. Update the cavity and body geometry.
4. Integrate the dynamic condition on the cavity to find ϕ^{n+1} on S_C .
5. Set the body and jet conditions for ϕ_n^{n+1} on S_B and S_J .
6. Solve mixed BVP to find $\phi_n^{n+1}, \phi_0^{n+1}$ on S_C and ϕ^{n+1} on S_B .

The continuous problem is discretized by a set of high-order B-spline patches that represent the geometry of the body and cavity and another set that represent the flow quantities of potential, ϕ , normal velocity, ϕ_n , and cavity displacement, h .

Third- to fifth-order splines and Galerkin schemes are used to spatially integrate both the cavity conditions and the mixed BVP. The use of a high-order discretization has been shown to be stable for the free-surface gravity wave problem where more typical flat panel methods have failed. Initial work with low-order, three-dimensional panel methods indicated that this would hold for cavity free-surface flows also.

The kinematic cavity condition is integrated in time using a forward (explicit) Euler method and the dynamic cavity condition is integrated in time using a backward (implicit) Euler method. For the dynamic condition, only the linear terms for the surface potential are treated implicitly. This mix of explicit and implicit methods was selected based on a stability analysis for wave propagation over discretized free surfaces.

The geometry and surface potential are represented by B-spline basis functions in space that overlap with their neighbors. These conditions produce a banded system of linear equations that must be solved at each time-step.

The unknown normal velocity on the cavity and potential on the body are obtained from the solution of the boundary integral equation, which contains the detachment and Kutta conditions. On the cavity, the disturbance potential at any instant is the sum of the known surface potential and an unknown additional potential.

The solution of the integral equation at each time-step represents the largest computational burden in the problem. To maintain high local accuracy and satisfy numerical stability requirements, a high-order, B-spline, Galerkin boundary-element method is used for this integral equation and two solvers are adopted. The first is a traditional dense matrix solver that requires $O(N^2)$ computational memory and operations. The second is an accelerated solver, using a precorrected fast Fourier transform (FFT) algorithm that is similar to the fast multipole method. This involves a sparse matrix requiring only $O(N)$ computational memory and operations.

Selected Results – General Flows

To date, the high-order boundary-element method has been adapted for the mixed BVP with the detachment and Kutta conditions. In Figure 11 an initial solution of the problem at the startup has been computed. In this figure, the high negative values of the normal velocity at the trailing end of the cavity show that the assumed geometry is too small and the cavity will lengthen along the side in the next time step. Work on the complete simulation is in progress.

This boundary-element method is numerically convergent, has been compared to analytic solutions for simple geometries, and has been validated experimentally in its original ship seakeeping manifestation, but it is too early to judge the performance of the cavity time-marching scheme and the wake sheet.

3.3 Cavitating Fins

In this section, we describe a tool used to predict the flow around cavitating fins, particularly fins with wedge-shaped cross-sections. The tool uses a boundary element method to predict six-degree-of-freedom forces for steady flight. The computed forces have been used as input to guidance and control simulations, as described below. The basic computational approach is summarized in Fine and Kinnas (1993).

A simple wedge-shaped fin geometry was considered for this investigation. It would be easily fabricated and appropriate to operation in the supercavitating regime, but is probably not optimal, although the wedge shape provides good strength characteristics. It is also convenient for comparison of the boundary-element results with preliminary predictions based on two-dimensional theory such as that of Uhlman (1987, 1989) or Wu (1956), or the various experimental data presented in May (1975). Also, for small wedge angles, the unsteady effects associated with the transition between partial cavitation and supercavitation are confined to a very limited range of deflection angles.

In computing the forces, a high level of detail was required over even the limited operational range considered, because several cavity detachment modes must be taken into account. The forces acting on cavitating fins are complicated by these different flow regimes. For wedge-shaped fins, four regimes must be considered. If the flow is symmetric about the symmetric fin, and the cavitation number is low enough, a cavity develops at the base of the wedge. Of course the fin does not develop lift in this case. At small angles of attack and moderately low cavitation numbers, a partial cavity develops at the leading edge separately from the base cavity. At larger angles of attack or lower cavitation numbers, the cavity originating at the leading edge becomes large enough to merge with the base cavity, forming a supercavity that envelopes all the surfaces except the pressure face. The lift curve slope in the supercavitating regime is less than in the partially cavitating regime. The final regime (which has not been modeled for the current effort) involves very high cavitation numbers. In that case, the cavities are eliminated and replaced with separation regions. The three regimes are shown in Figure 12.

Brief Description of LScav

ETC's Lifting Surface Cavitation code (LScav) computes the first iteration of the fully nonlinear cavity solution for a general three-dimensional wing attached to a non-lifting "center-body" at arbitrary cavitation number. The flow is assumed to be steady, inviscid, incompressible, and irrotational (outside of a thin vortex sheet trailing behind the lifting surface). The solution is found by applying a disturbance-potential-based panel method that involves a numerical solution of Green's third identity. The method is described in the context of cavitating propellers in Fine (1992).

The wing and center-body are assumed to be symmetric about a vertical plane intersecting the body centerline. The cavity solution represents the first iteration of a fully nonlinear solution. In order to understand the difference between the first iteration solution and the fully nonlinear solution, consider a two-dimensional hydrofoil and assume that the cavity length is known. Since the cavity length is a single-valued function of the cavitation number for all stable two-dimensional cavities, the cavitation number may not be specified in this canonical problem and, in fact, must be

considered an unknown to be determined as part of the solution. To solve the nonlinear problem, one must first guess the location of the cavity boundary and satisfy the boundary conditions on that approximate surface. However, since we cannot say beforehand that our approximate location of the cavity boundary is the correct one, we can only satisfy the dynamic boundary condition (the condition that the pressure be constant on the boundary and equal to the cavity pressure) in the solution. In general, the kinematic boundary condition (the condition that the normal velocity vanish on the cavity surface) will not be satisfied. However, we may use the kinematic boundary condition to update the location of the cavity surface.

Since the first guess of the cavity location is arbitrary, it is numerically convenient to first solve the boundary conditions on the wing surface and, for supercavities, on a zero-thickness sheet downstream of the wing. To find the nonlinear solution, one simply re-solves the problem with the new body shape defined from the first iteration (see Figure 13). The fully nonlinear solution is found when the solution converges to some preset tolerance. In previous work (Fine, 1992), extensive studies showed that the accuracy of the first iteration solution relative to the fully nonlinear solution was very good over a reasonably large range of operating conditions. As a result (and motivated by the significant computational savings of solving only the first iteration) LScav was configured to compute only the first iteration of the nonlinear solution.

Sample LScav results are shown in Figure 14, which indicates the convergence of the cavity planform for a fin with a triangular planform and a wedge-shaped cross-section. Table 1 shows the convergence of the corresponding lift and drag coefficients and the cavity volume. Convergence to three significant digits occurs with about 1300 total panels. The total amount of memory that is required for this size problem is roughly 108 MB.

LScav has been validated through comparison of computed lift and drag coefficients to measurements made in a water tunnel. A sample of the validation is shown in Figure 15.

4 APPLICATION OF SLENDER-BODY-THEORY

This section is based on Varghese, et al, (1997).

In slender-body theory (SBT), the slenderness ratio, ϵ , of the body is defined as the ratio of the maximum radius to the total length. It is assumed that $\epsilon \ll 1$ and that the cavitation number and the inverse square of the Froude number are of order $\epsilon^2 \ln \epsilon$ (Chou, 1974). The axial gradient of the body-cavity radius should be of the same order as the slenderness parameter, restricting the analysis to certain classes of cavitators using this approach.

In the following sections, Chou's formulation is extended to subsonic compressible fluid flows. Also presented are selected results for an incompressible fluid. Chou's original method incorporated terms accounting for an axisymmetric gravitational field, and these have been retained in the following presentation. Results may be found in Varghese, et al, (1997).

4.1 Mathematical Formulation

The present SBT analysis assumes an axisymmetric body with a conical cavity closure. A salient cavity detachment point is specified in the model as is shown in Figure 16. The free-stream velocity, U_∞ , is at zero angle of attack. The body length is ℓ_b , the cavity length is ℓ_c , and the total length is ℓ . In the following formulation, all lengths are made dimensionless with body length, velocities with free stream velocity, and potential with body length and free stream velocity.

Incompressible Flow

The total potential is

$$\Phi = x + \phi, \quad (4.1)$$

where ϕ is the perturbation velocity potential. The axial and radial components of the perturbation velocity are

$$u_x = \frac{\partial \phi}{\partial x} \quad \text{and} \quad u_r = \frac{\partial \phi}{\partial r}, \quad (4.2)$$

respectively.

The SBT outer expansion results in Laplace's equation for the perturbation potential:

$$\phi(x, r) + \frac{\phi_r}{r} + \phi_{rr} = 0. \quad (4.3)$$

For a continuous distribution of sources along the x -axis, the solution for equation 4.3 can be written as

$$\phi(x, r) = -\frac{1}{4\pi} \int_0^\ell \frac{q(\xi) d\xi}{\sqrt{(x-\xi)^2 + r^2}}, \quad (4.4)$$

where $q(\xi)$ is the source strength defined along the axis at location ξ . From the SBT inner expansion, assuming $db/dx = O(\epsilon)$, the source strength is

$$q(x) = \pi \frac{d(b^2)}{dx} \quad (4.5)$$

The kinematic boundary condition,

$$u_r = \frac{db}{dx}, \quad (4.6)$$

is formed from the no-flux condition on the body and cavity surfaces. The cavity pressure is assumed to be constant. The dynamic boundary condition is derived from Bernoulli's equation:

$$\sigma = -C_p = 2u_x + u_r^2 - \frac{2(x-1)}{F_b^2}. \quad (4.7)$$

Here, σ is the cavitation number, C_p , is the pressure coefficient, and

$$F_b = \frac{\Delta U_\infty}{\sqrt{g\ell_b}}$$

is the Froude number based on body length. Here g is the gravitational acceleration.

Let $\zeta_b = b_b^2$ and $\zeta_c = b_c^2$. Substituting expressions for the radial and axial velocity components defined at the body-cavity surface, in the dynamic boundary condition, equation 4.7, results in a non-linear integro-differential equation:

$$\sigma = \frac{1}{2\pi} \int_0^\ell \frac{q(\xi)(x-\xi)d\xi}{[(x-\xi)^2 + \zeta_c]^{\frac{3}{2}}} + \left(\frac{db_c}{dx}\right)^2 - \frac{2(x-1)}{F_b^2}, \quad 1 \leq x \leq \ell, \quad (4.8)$$

where b_c is the cavity radius. Integrating by parts and using equation 4.5 for the source strength yields (Chou, 1974):

$$\frac{1}{2} \int_1^\ell \frac{\frac{d^2\zeta_c}{d\xi^2} d\xi}{\sqrt{(x-\xi)^2 + \zeta_c}} = -\sigma - \frac{1}{2} \int_0^1 \frac{\frac{d^2\zeta_b}{d\xi^2} d\xi}{\sqrt{(x-\xi)^2 + \zeta_c}} + \frac{\frac{d\zeta_c}{dx} \Big|_1}{\sqrt{(x-\ell)^2 + \zeta_c}} - \frac{\frac{d\zeta_b}{dx} \Big|_0}{\sqrt{x^2 + \zeta_c}} + \left(\frac{db_c}{dx}\right)^2 - \frac{2(x-1)}{F_b^2}. \quad (4.9)$$

With the assumption that the cavity closes as a cone, the above equation can be written for a conical body as:

$$\frac{1}{2} \int_1^\ell \frac{\frac{d^2\zeta_c}{d\xi^2} d\xi}{\sqrt{(x-\xi)^2 + \zeta_c}} = - \left[\sigma + \frac{1}{2} \int_0^1 \frac{\frac{d^2\zeta_b}{d\xi^2} d\xi}{\sqrt{(x-\xi)^2 + \zeta_c}} - \frac{\left(\frac{d\zeta_c}{dx}\right)^2}{4\zeta_c^2} + \frac{2(x-1)}{F_b^2} \right]. \quad (4.10)$$

In this equation, the right hand side is known for a given cavity shape. In the current approach, the cavity shape is approximated and updated iteratively. With an assumed initial cavity shape, equation 4.10 is solved for a new cavity shape. For that procedure, the cavity axial length is discretized into n panels. In each panel, a locally quadratic polynomial is used to approximate ζ_c . Varghese, et al, (1997) presents the details of building and solving a system of equations to update the discretized cavity geometry.

Pressure and Drag Coefficients for the Case of an Incompressible Fluid

Upon convergence, the pressure coefficient along the body is computed as follows:

$$C_p(x) = -\frac{1}{2} \int_0^x \frac{\frac{d\zeta}{d\xi}(x-\xi)d\xi}{\left[(x-\xi)^2 + \zeta_b^2\right]^{\frac{3}{2}}} - \left(\frac{db_b}{dx}\right)^2 + \frac{2(x-1)}{F_b^2}, \quad 0 \leq x \leq 1. \quad (4.11)$$

The pressure coefficient along the cavity is the negative of the cavitation number. The base drag coefficient, based on the maximum body cross-sectional area, is found by integrating the pressure coefficients over the body:

$$C_{db} = \frac{1}{\zeta_b(1)} \int_0^1 C_p(x) \frac{d\zeta_b}{dx} dx + \sigma. \quad (4.12)$$

In Varghese, et al, (1997), viscous drag corrections for axisymmetric bodies were developed based on three different methods: (1) Thwaites' method with a linear velocity profile; (2) Thwaites' method with a shear function; and, (3) the method of Falkner and Skan. Moderate improvement to the comparison of the predicted total cavitator drag to experimental data was obtained for certain cases.

Subsonic Compressible Flow

In this section we extend the previous formulation to the case of compressible flows. Results may be found in Varghese, et al, (1997). A method is proposed in Kirschner, et al, (1995) for extending the axisymmetric boundary-element method presented above to compressible subsonic flows.

The outer expansion for the perturbation potential for slender bodies in a compressible fluid results in the following governing equation (Ashley and Landahl, 1965):

$$(1 - M_\infty^2) \phi_{\hat{x}\hat{x}} + \frac{\phi_{\hat{r}}}{\hat{r}} + \phi_{\hat{r}\hat{r}} = 0, \quad (4.13)$$

where the hatted variables represent the physical coordinate for the subsonic flows. With a transformation to $x = \hat{x}$ and $r = \beta \hat{r}$ where $\beta = \sqrt{1 - M_\infty^2}$, equation 4.13 reduces to Laplace's equation. Thus the solution for a continuous source distribution is

$$\phi(x, r) = -\frac{1}{4\pi} \int_0^\ell \frac{q(\xi) d\xi}{\sqrt{(x-\xi)^2 + \beta^2 r^2}}. \quad (4.14)$$

Here $q(x)$ is defined by equation 4.5. The radial velocity component is given by equation 4.6. However, the axial velocity component depends on β as follows:

$$u_x(x, r) = \frac{1}{4\pi} \int_0^\ell \frac{q(\xi)(x-\xi) d\xi}{\left[(x-\xi)^2 + \beta^2 r^2\right]^{\frac{3}{2}}}. \quad (4.15)$$

With the constant cavity pressure assumption, the dynamic boundary condition is derived from the compressible Bernoulli equation:

$$\sigma = \frac{2}{\gamma M_\infty^2} \left\{ 1 - \left[1 - (\gamma - 1) M_\infty^2 \left(u_x + \frac{u_r^2}{2} \right) \right]^{\frac{\gamma}{\gamma-1}} \right\}. \quad (4.16)$$

As for the case of incompressible flow, substitution of equations 4.6 and 4.15 respectively for the radial and the axial velocity components of equation 4.16 yields an integro-differential equation:

$$\left[1 - \frac{\gamma M_\infty^2}{2} \sigma \right]^{\frac{\gamma-1}{\gamma}} = 1 - (\gamma - 1) M_\infty^2 \left[\frac{1}{4\pi} \int_0^\ell \frac{q(\xi)(x-\xi)}{[(x-\xi)^2 + \beta^2 \zeta_c]^{\frac{3}{2}}} d\xi + \frac{1}{2} \left(\frac{db_c}{dx} \right)^2 \right], \quad 1 \leq x \leq \ell, \quad (4.17)$$

Integrating by parts and substituting equation 4.5 for the source strength, the governing equation becomes

$$\begin{aligned} \int_1^\ell \frac{\frac{d^2 \zeta_c}{d\xi^2} d\xi}{\sqrt{(x-\xi)^2 + \beta^2 \zeta_c}} &= \frac{4}{(\gamma - 1) M_\infty^2} \left\{ \left[1 - \frac{\gamma M_\infty^2}{2} \sigma \right]^{\frac{\gamma-1}{\gamma}} - 1 \right\} \\ &\quad - \int_0^1 \frac{\frac{d^2 \zeta_b}{d\xi^2} d\xi}{\sqrt{(x-\xi)^2 + \beta^2 \zeta_c}} - \frac{\frac{d\zeta_c}{dx} \Big|_\ell}{\sqrt{(x-\ell)^2 + \beta^2 \zeta_c}} + \frac{\frac{d\zeta_b}{dx} \Big|_0}{\sqrt{x^2 + \beta^2 \zeta_c}} + \left(\frac{db_c}{dx} \right)^2 \end{aligned} \quad (4.18)$$

For a conical body with a conical cavity closure, this equation becomes

$$\int_1^\ell \frac{\frac{d^2 \zeta_c}{d\xi^2} d\xi}{\sqrt{(x-\xi)^2 + \beta^2 \zeta_c}} = \frac{4}{(\gamma - 1) M_\infty^2} \left\{ \left[1 - \frac{\gamma M_\infty^2}{2} \sigma \right]^{\frac{\gamma-1}{\gamma}} - 1 \right\} - \int_0^1 \frac{\frac{d^2 \zeta_c}{d\xi^2}}{\sqrt{(x-\xi)^2 + \beta^2 \zeta_c}} d\xi + \frac{\left(\frac{d\zeta_c}{dx} \right)^2}{2\zeta_c}. \quad (4.19)$$

Pressure and Drag Coefficients for the Case of a Compressible Fluid

The pressure coefficient along the body is given by

$$\frac{\gamma M_\infty^2}{2} C_p(x) = \left[1 - (\gamma - 1) M_\infty^2 \left(\frac{1}{4} \int_0^\ell \frac{\frac{d\zeta_b}{d\xi} (x-\xi) d\xi}{[(x-\xi)^2 + \beta^2 \zeta_b]^{\frac{3}{2}}} + \frac{1}{2} \left(\frac{db_b}{dx} \right)^2 \right) \right]^{\frac{\gamma}{\gamma-1}} - 1, \quad 0 \leq x \leq 1. \quad (4.20)$$

Using this form to compute the pressure coefficient, the base drag coefficient, C_{db} , for the compressible case can be calculated using equation 4.12.

4.2 Selected Results – Slender Body Theory

The SBT model was used to predict supercavitating flows of both compressible and incompressible fluids at various cavitation numbers. All the results shown here are for a 10°-cone angle. The cavity shapes (scaled to show cavities enlarged in the radial direction) for cavitation numbers ranging from 0.005 to 0.05 are shown in Figure 17 for the incompressible case. The cavity length increases as the cavitation number decreases, as expected. The predicted surface pressure distributions are plotted in Figure 18 for different cavitation numbers. This quantity decreases as the cavitation number increases. Results have been compared with curve fits of empirical data (May, 1975). In Figure 19, the maximum cavity radius has been plotted, made dimensionless with

respect to the radius at cavity detachment. Figure 19 illustrates an excellent match with experimental values, particularly at low cavitation numbers where SBT is more valid.

4.3 Summary – SBT

Formulations have been presented for applying Chou's SBT model to both incompressible and compressible flows. Selected results have been presented for the incompressible case. Some comparison with experimental data has been presented.

In Varghese, et al, (1997), additional formulation, results, discussion, and comparison are presented for the effects of both an axisymmetric gravity field and viscous drag.

5 NUMERICAL FLIGHT AND CONTROL SYSTEM SIMULATION

In this section, which is based on Kirschner, et al, (2001), we describe numerical flight simulation for supercavitating vehicles. We first discuss the nonlinear forces acting on the cavitator, the fins (if present), and any portions of the hull that penetrate the cavity boundary during excursions from the fully-enveloped condition. Next, we describe simulation of vehicle flight, including system stability and system performance during execution of a banked turn. Without control, some vehicle configurations can be unstable, whereas a feedforward-feedback strategy can control some configurations over a range of turn rates.

5.1 Hydrodynamical Model

The behavior of the cavity is central to the dynamics of a supercavitating vehicle. The nominally steady cavity behavior forms the basis of the quasi-time-dependent model implemented for the current investigation. This model affects not only the forces acting at the nose of the vehicle, but also the immersion of the fins and any planing forces due to contact between the body and the cavity boundary. It is the cavity that makes this dynamical system not only nonlinear, but also dependent on strong memory effects that link the history of motion to the instantaneous cavity shape.

The three parameters that characterize time-averaged or quasi-steady ventilated flows are the cavitation number, the cavity Froude number, and the ventilation coefficient. The cavitation number is defined in equation 2.11, and has been discussed extensively in the formulations above. The cavity Froude number (not to be confused with the related Froude number based on body length discussed above) and the ventilation coefficient are defined as

$$\mathcal{F} = \frac{V}{\sqrt{gd_c}} \quad (5.1)$$

and

$$C_Q = \frac{Q}{Vd_c^2}, \quad (5.2)$$

respectively. Again, g is the gravitational acceleration. The cavitator diameter is d_c . p_∞ and p_c are the ambient and cavity pressures, respectively. V is the vehicle velocity and Q is the volumetric rate at which ventilation gas is supplied to the cavity. The cavitation number expresses the tendency of cavitation to occur in a flow, and is thus a principal quantity governing cavity dimensions. The Froude number characterizes the importance of gravity to the flow, and therefore governs distortions from a nominally axisymmetrical shape. The ventilation coefficient governs the time-dependent behavior of the cavity as ventilation gas is entrained by the flow.

For the horizontal trajectories considered in these lecture notes, the cavitation number is very low (on the order of 0.015 to 0.030) and the cavity Froude number is typically rather high (on the order of 50 to 100). The cavity is slender, and its maximum diameter is at least 5 times greater than the cavitator diameter. Cavity tail-up under the influence of gravity is small, but not insignificant to the vehicle design.

The nomenclature used for basic vehicle dynamics during the remainder of these lecture notes is presented in Figure 20. The x -axis is directed forward along the nominal vehicle long axis, y is to starboard, and z completes an orthogonal system obeying the right-hand rule. The origin of this coordinate system is located at the cavitator pivot point. Following Kiceniuk (1954), the following relationships have been employed to estimate the hydrodynamic forces and moment acting on the circular disk cavitator selected for investigation:

$$\begin{aligned} C_D(\sigma, \alpha_c) &= \frac{D_c(\sigma, \alpha_c)}{1/2 \rho V^2 A_c} \cong C_{D0}(1 + \sigma) \cos^2 \alpha_c \\ C_L(\sigma, \alpha_c) &= \frac{L_c(\sigma, \alpha_c)}{1/2 \rho V^2 A_c} \cong C_{D0}(1 + \sigma) \cos \alpha_c \sin \alpha_c \\ C_M(\sigma, \alpha_c) &= \frac{M_c(\sigma, \alpha_c)}{1/2 \rho V^2 d_c A_c} \cong 0 \end{aligned} \quad (5.3)$$

where D_c and L_c are the drag and lift forces acting on the cavitator, M_c is the hydrodynamic moment, and A_c is the disk area. The drag coefficient at zero angle of attack and cavitation number, C_{D0} , is taken as approximately 0.805 based on empirical data (May, 1975).

Various analytical, numerical, and semi- and fully-empirical models have been developed that provide estimates of the maximum cavity diameter, d_{\max} , and the cavity length, ℓ_c . The analytical formulae of Garabedian (1956) provide useful and reasonably accurate approximations for investigation of vehicle dynamics:

$$\frac{d_{\max}}{d_c} = \sqrt{\frac{C_D(\sigma, 0)}{\sigma}} \quad (5.4)$$

and,

$$\frac{\ell_c}{d_c} = \sqrt{\frac{C_D(\sigma, 0)}{\sigma} \ln \frac{1}{\sigma}} \quad (5.5)$$

For purposes of time-domain simulation of vehicle dynamics, it is desirable to use simple models. In a cylindrical-polar system with coordinates x , r , and θ , the nominal axisymmetric shape can be approximated as:

$$\frac{r_c}{d_c} = \frac{d_{\max}}{2d_c} \left[1 - \left(\frac{x/d_c - \ell_c/2d_c}{\ell_c/2d_c} \right)^2 \right]^{1/2.4} \quad (5.6)$$

where $r_c(x, \theta)$ is the cavity offset (Münzer and Reichardt, 1950, derived from a low-order potential flow model).

The effects of gravity and turning on this generalized ellipsoidal cavity shape can be approximated as a distortion of the line of centers (y_c, z_c) , described by

$$y_c(x) = \mp \frac{1}{\xi^2} \frac{a_{\text{turn}}}{g} \left(\frac{x}{d_c} \right)^2 \quad (5.7a)$$

and

$$z_c(x) = -\frac{1}{\xi^2} \frac{a_g}{g} \left(\frac{x}{d_c} \right)^2 \quad (5.7b)$$

where a_{turn} is the turn acceleration and a_g is the tail-up acceleration of the cavity, here approximated using the semi-empirical formula recommended by Waid (1957). A binomial expansion (retaining the second term) has been used to simplify the term associated with turning, applying the principle of independent development of cavity sections (Logvinovich, 1985) and assuming that the cavitator traces a circular path in a horizontal plane. Although the distortion of the cavity line of centers due to turning and gravity has been considered, distortions associated with cavitator lift have been ignored. Cavity foreshortening has also been neglected, and distortions of the cavity sections from their nominal circular shapes have been ignored for the current investigation. Under these assumptions, the cavity locus of section centers is coincident with the cavitator trajectory.

Equations 5.7 apply to a steady horizontal turn with gravity acting in the vertical direction. Although generalization to more complicated trajectories would not be difficult, the current formula provides insight concerning the behavior and limitations of a supercavitating vehicle in a turn. The consistent formulation shows the relative influences of turning and gravity, both of which become increasingly important at low cavity Froude numbers. To the order of terms retained in equations 5.7, the locus of cavity section centers is quadratic in the axial coordinate.

The importance of cavity distortion in high turn rates is apparent in Figure 21, which presents results for an extreme turn (in this case, a 5-g turn that is probably impractical, but is illustrative of the cavity-body interactions important to the problem). The nonlinear behavior is clear from this figure. Firstly, as the cavity distorts from a nominally axisymmetric configuration, the immersion of the fins into the ambient liquid outside the cavity becomes asymmetric. Therefore, the couple associated with symmetric or anti-symmetric fin trim will result in nonlinear system response. Secondly, a system designed for close envelopment of the vehicle by a nominally axisymmetric cavity (or even one designed for cavity tail-up in straight and level flight) will be subject to nonlinear forces associated with afterbody planing.

Only the most essential aspects of the unsteady hydrodynamics have been modeled. Self-pulsation of the cavity has been ignored, but changes in cavity shape due to cavitator motion have been taken into account via a convolution scheme. The fin forces are evaluated at each time step via a look-up algorithm. Thus, the three basic cavitating fin flow regimes (base- and partially cavitating and supercavitating) contribute to the unsteady fin forces, but various higher-order hydrodynamic effects in the evolution of the fin cavity are not modeled. Most importantly, hydrodynamic added mass effects have been ignored.

Secondary flows – notably, those due to the fins and to afterbody planing – have been ignored in the current effort, although the theory used to estimate the afterbody planing forces accounts for the lowest-order effect of the spray jet.

In the nominal condition of straight and level flight, the supercavitating vehicle configurations of interest in these lecture notes are supported in the vertical direction by a lift force acting on the cavitator and by a combination of planing and lift on the fins near the after end of the vehicle. The optimal support by afterbody planing forces has not yet been determined with certainty, although the results presented below are enlightening. This secondary function of the cavitator as a lifting surface is essential to operation of a supercavitating vehicle. Since virtually no lift is provided by the gas-enveloped hull, the vehicle weight must be supported by the control surfaces both forward and aft of the mass center. It is natural to provide the forward lift vector by orienting the cavitator at an appropriate angle of attack. Moreover, accounting for changes in vehicle mass and mass center as fuel is consumed, and maintaining optimal vehicle orientation with respect to the cavity during a maneuver, require that this trim angle be variable and controlled.

The forces acting on the fins were predicted using a fully three-dimensional boundary-element method of the type described above, supplemented with a viscous drag correction.

Afterbody forces in the case where planing on the cavity surface occurs were computed using an extension of Wagner planing theory developed by Logvinovich (for example, 1980). The cavity

in way of the planing region is approximated as a cylindrical free surface. The pressure force normal to the inclined longitudinal axis of the cylindrical hull is given by

$$F_b = \pi \rho \bar{r}_c^2 V^2 \sin \bar{\alpha}_b \cos \bar{\alpha}_b \frac{r_b + h_0}{r_b + 2h_0} \left(1 - \left(\frac{\Delta}{h_0 + \Delta} \right)^2 \right), \quad (5.8)$$

where: r_b is the hull radius (assumed to be constant over the planing region); \bar{r}_c , $\bar{\alpha}_b$, and Δ are (respectively) the cavity radius, the angle of attack between the longitudinal axes of the body and the cavity, and the difference between the cavity and hull radii (all averaged along the planing region); and h_0 is the immersion depth at the transom measured normal to the cavity centerline. Similarly, the moment of pressure forces about the transom can be expressed as

$$M_0 = \pi \rho \bar{r}_c^2 V^2 \cos^2 \bar{\alpha}_b \frac{r_b + h_0}{r_b + 2h_0} \frac{h_0^2}{h_0 + \Delta}. \quad (5.9)$$

A viscous drag correction was applied for the current investigation. Forces on the blast tube were neglected, since the fluid outside the time-averaged cavity boundary in that region is characterized by a significant void fraction, so that the overall planing forces acting on the reduced sectional area are expected to be rather small.

5.2 Candidate Vehicle Configuration

Several design issues must be addressed to completely understand the dynamics and control of supercavitating vehicles. One concern is the optimal allocation of fin lift relative to planing force to support the vehicle afterbody. A related question is the need for fin support: if stable flight can be maintained with the afterbody completely supported by the planing force, the elevators and their attendant drag and complexity become unnecessary.

Simulation was conducted on a vehicle with the following characteristics: 4.0 m in length, 0.2 m in diameter, and with a cavitator diameter of 0.07 m. The fins were located 3.5 m aft of the cavitator, and were swept back 15°. Although the mass properties of the vehicle will change as the rocket and ventilation fuels are consumed, they were assumed constant for purposes of the current analysis. A cruciform fin arrangement has been assumed: A pair of horizontal elevators provide some component of steady lift to support the afterbody and would be important to depth changes, while a pair of vertical rudders stabilize the vehicle in roll, but are otherwise deflected only during maneuvers.

As is discussed in Kirschner (2001), under certain conditions, a banked maneuvering strategy might be advantageous for a self-propelled supercavitating vehicle. This strategy was adopted for the investigation described herein.

5.3 Simulation of Underwater Flight

The current investigation focused on the simplified system of Figure 22, for which high frequency hydrodynamic noise excitation and other noise sources have been ignored. Moreover, it is assumed that knowledge of the system state is accurate, eliminating the requirement for a state estimator. However, the nonlinearity of the vehicle-cavity system has been retained. Nonlinearity enters the system via the vehicle, fin, and cavity behavior, due both to the nonlinear force coefficients and to memory effects associated with cavity evolution. Control has been implemented via a linear-quadratic regulator (LQR). Cavity memory effects and the discontinuities in the force coefficients require incorporation of the feedforward model (discussed below) to maintain acceptable system performance.

For the simplified system, the input to the regulator is the error vector, $\mathbf{x} = \mathbf{x}_d - \mathbf{y}$, computed as the difference between the commanded state vector, \mathbf{x}_d , and the corresponding actual state vector, \mathbf{y} . Both the actual and commanded state vectors have the form

$$\left\{ \begin{array}{cccccc} x & y & z & \phi & \theta & \psi \\ \text{surge} & \text{sway} & \text{heave} & \text{roll} & \text{pitch} & \text{yaw} \end{array} \right\} \leftarrow \text{displacements}$$

$$\text{rates} \rightarrow \left\{ \begin{array}{cccccc} u & v & w & p & q & r \\ \text{surge} & \text{sway} & \text{heave} & \text{roll} & \text{pitch} & \text{yaw} \end{array} \right\}^T$$

However, several of these states might not be measured on a vehicle. Thus, for the simulations discussed below, several of the state variables were eliminated from the system. Typically, a 7-state system was investigated, assuming that both rates and displacements in roll, pitch, and yaw are available from an inertial measurement unit and that some measurement of vehicle depth, z , can be obtained.

A classical regulator would provide a control vector, \mathbf{u} , directly to the hydrodynamic control effectors (in this case, the fins and the cavitator):

$$\mathbf{u} = \begin{Bmatrix} u_1 & u_2 & u_3 & u_4 & u_5 \\ \text{starboard} & \text{lower} & \text{port} & \text{upper} & \text{cavitator} \end{Bmatrix}^T \quad (5.10)$$

However, the control vector of interest involves both the feedback output from the LQR, \mathbf{u}_b , and output from the feedforward model, \mathbf{u}_f :

$$\mathbf{u} = \mathbf{u}_b + \mathbf{u}_f \quad (5.11)$$

Prior to flight simulation of a supercavitating body, the thrust and nominal speed are specified. Values of the state and control vectors are then determined for four basic flow conditions:

- Two trim conditions: fin-supported with pitch equal to zero, and planing-supported with fin deflection (relative to the vehicle axis) equal to zero; and, for each trim condition,
- Two maneuvering conditions: straight and level flight, and level turning at a specified constant turn rate.

Determination of these equilibrium conditions involves a nonlinear root search. In consideration of the discontinuity that can occur at the angle where planing first occurs, a Nelder-Mead scheme has been adopted.

The feedforward model investigated in this effort is specialized for supercavitating vehicle dynamics. A scheme has been selected for which the system is regulated about one of four distinct fixed points. The point selected depends on the user-specified operating condition. The first two fixed points are defined by the nominal condition of straight-line flight for either fin or planing support of the afterbody. The other two are similar, except that they are selected as equilibrium conditions for steady turning in the horizontal plane. Thus the output from the feedforward model is

$$\mathbf{u}_f \in \begin{cases} \mathbf{u}_1 & \text{fin supported, zero pitch, straight flight} \\ \mathbf{u}_2 & \text{planing, zero fin deflection, straight flight} \\ \mathbf{u}_3 & \text{fin supported, banking pitch, turn rate } a_{\text{turn}} \\ \mathbf{u}_4 & \text{planing, zero fin deflection, turn rate } a_{\text{turn}} \end{cases} \quad (5.12)$$

and feedback control is optimized to regulate motion about one of these equilibrium conditions as the vehicle traverses its commanded trajectory.

The nonlinear equation of motion involves not only the present state, but also the history of cavitator motion, $\mathbf{c}(t)$:

$$\begin{aligned} \dot{\mathbf{x}} &= \mathbf{f}(\mathbf{x}, \mathbf{c}(t - \tau), \mathbf{u}) \\ \mathbf{y} &= \mathbf{g}(\mathbf{x}) \end{aligned}$$

where τ represents the delay between motion at the cavitator and action along the afterbody. For each flow condition, s , the state-space model for the simplified system is defined in the usual manner as:

$$\begin{aligned} \dot{\mathbf{x}} &= \mathbf{A}_s \mathbf{x} + \mathbf{B}_s \mathbf{u} \\ \mathbf{y} &= \mathbf{C}_s \mathbf{x} + \mathbf{D}_s \mathbf{u} \end{aligned} \quad s \in \{1, \dots, 4\} \quad (5.13)$$

The Jacobian matrices are computed numerically prior to flight simulation as (for example)

$$A_{ij} = \frac{\partial f_i}{\partial x_j} \quad s \in \{1, \dots, 4\} \quad (5.14)$$

where the indices i and j vary from 1 through 12 for the complete state vector and from 1 through 5 for the control vector in each flow condition. For the simplified system, the Jacobian matrices in the second of equations 5.13 are simply

$$\mathbf{C}_s = \mathbf{I} \quad s \in \{1, \dots, 4\} \quad (5.15)$$

(the identity matrix), and

$$\mathbf{D}_s = \mathbf{0} \quad s \in \{1, \dots, 4\} \quad (5.16)$$

Regulation for the general LQR is measured by the quadratic performance criterion

$$J(\mathbf{u}) = \int_{t=0}^{\infty} \left(\mathbf{x}^T \mathbf{Q} \mathbf{x} + 2 \mathbf{x}^T \mathbf{N} \mathbf{u}_b + \mathbf{u}_b^T \mathbf{R} \mathbf{u}_b \right) dt \quad (5.17)$$

where the user-specified weighting matrices, \mathbf{Q} , \mathbf{N} , and \mathbf{R} , define the trade-off between regulation performance and control effort. For the current investigation, the cross-weighting matrix \mathbf{N} was taken as zero, as were all off-diagonal elements of the state and control weighting matrices, \mathbf{Q} and \mathbf{R} . A MATLAB[®] Control System Toolbox routine is used to determine the gain matrices, \mathbf{K}_s , that minimize the cost function, $J(\mathbf{u})$, for use in the state feedforward-feedback control law (MATH WORKS, 1998) for each of the 4 fixed points considered. The control law is then expressed as:

$$\mathbf{u} = \mathbf{u}_{fs} - \mathbf{K}_s \mathbf{x} \quad s \in \{1, \dots, 4\} \quad (5.18)$$

A substantial effort was devoted to testing various combinations of the weighting matrices \mathbf{Q} and \mathbf{R} to achieve acceptable performance, although a more systematic and rigorous effort is warranted. The weighting and gain matrices are all computed prior to flight simulation.

A 4th-order Runge-Kutta scheme was used to integrate the equations of motion in time. At each time step the cavity geometry is updated to account for the motion of the cavitator. The forces acting on the cavitator, fins, and afterbody are then updated, and vehicle accelerations in each of the 6 degrees of freedom are computed. The state and error vectors are updated. The control vector is then updated using the gain matrix appropriate to the specified desired operational condition and the control equation is applied.

5.4 Selected Results - Simulations

For all cases discussed below, the operating speed and cavitation number were 75 m/s and 0.03, respectively.

Figure 23 shows the total lift margin (the difference between the total lift and the vehicle weight) as a function of vehicle pitch and elevator deflection angle. The cavitator angle for each curve was selected to provide equilibrium for a pitch angle of zero. Equilibrium is achieved in the fin-supported case at elevator deflection angles between approximately 0.30° and 0.55°; below elevator deflection angles or approximately 0.30° the afterbody is primarily supported by planing forces. Note the discontinuity in lift curve slope when afterbody planing first occurs (at a pitch angle of approximately 0.23°); this represents a tremendous increase in the effective system stiffness and the characteristic response frequencies. The small fin deflections required to produce a substantial change in the forces acting on the body might present an additional challenge for control.

The open- and closed-loop eigenvalues of the system, linearized about the fixed points associated with the fin and planing supported cases for straight-line flight, are shown in Figure 24. For both types of afterbody support, the uncontrolled system has one unstable mode. Preliminary analysis suggests that this is a corkscrew motion associated with cavity tail-up under the influence of gravity: roll and sway are unstably coupled due to asymmetry in the fin immersion as the body rolls about its long axis, which is eccentrically located with respect to the line of cavity centers in way of the fins. This effect can be eliminated in the controlled system, provided some measurement of depth is available; if not, the unstable mode is present even for the controlled system. As expected, the most important remaining difference between the controlled and uncontrolled systems is a significant increase in the damping of each mode in the controlled case. Similarly, the primary difference between the fin and planing supported cases is a significant increase in the frequency of the oscillatory modes in the planing supported case. In all cases, several lightly damped modes are present.

The vehicle motion predicted by time-domain simulation of free decay in pitch for the fin-supported case in straight and level flight is presented in Figure 25. Two types of behavior are presented: essentially linear behavior associated with a small initial pitch rate perturbation of 1°/s, and the clearly nonlinear behavior due to a large perturbation of 20°/s. In both cases, control is required to recover from the perturbation and return to the original depth. More interestingly, the

linear behavior is non-oscillatory for both the controlled and uncontrolled cases, whereas, in the nonlinear case, the perturbation initiates a rather violent pitch oscillation at a frequency of approximately 9.5 Hz that is modulated by a second, gentler, higher-frequency oscillation. The shapes of the peaks and troughs indicate that the vehicle is skipping off the bottom of the cavity in the nonlinear case.

Simulation of vehicle motion in steady, planing-supported, straight and level flight predicts behavior such as that shown in Figure 26. It can be seen that pitch increases with time, but that a 7-state controller both eliminates the tendency of the vehicle to dive and reduces the violent tail-slap behavior. The frequencies characterizing the two types of response are markedly different: the uncontrolled case is dominated by a relatively long-period skipping mode, whereas control eliminates this mode, leaving the higher modulating frequency. The planing force history indicates that skipping occurs in both cases – apparently the controlled response during the planing portion of the cycle is sufficient to mitigate the unsteady cavity behavior in such a manner that the afterbody excursions are not so extreme.

5.5 Summary – Simulation

This section presented strategies for the control of the highly coupled nonlinear system comprising a supercavitating vehicle. A simple hydrodynamic model was implemented for simulating the behavior of such a system. In consideration of the nature of the forces acting on a gas-enveloped body, and in order to maintain mechanical simplicity of the cavitator, a banked maneuvering strategy was investigated. Results of dynamical simulation for a specific vehicle were presented both for uncontrolled flight and with LQR-based feedforward-feedback control.

The system behavior is dominated by the distinct change in the nature of the forces as the afterbody moves between a planing and a non-planing condition. The system eigenvalues strongly depend on the type of afterbody support specified for vehicle operation, but that (under the assumptions made for the simplified hydrodynamics model) a 7-state controller can eliminate the most undesirable behavior in either case. Additional discussion, including description of the simulation of banked maneuvers in steady turns, may be found in Kirschner, et al, (2001).

ACKNOWLEDGEMENTS

The authors are very grateful to Dr. Kam Ng (Office of Naval Research, ONR), who supported the development and presentation of these lecture notes. Many other sponsors supported the work presented herein, including Mr. James Fein (then of ONR), Drs. William Carey and Theo Kooij (formerly and currently of the Defense Advanced Research Projects Agency, DARPA), Dr. Stuart Dickinson (then manager of the NUWC Independent Research Program), and Mr. Bernard Myers (then manager of the NUWC Bid and Proposal Program).

Dr. Abraham Varghese (Naval Undersea Warfare Center, NUWC) participated in the development of many of the computation tools presented herein. Dr. Scott Hassan (NUWC) contributed to the afterbody planing model used in the dynamical simulations. The fin force measurements used to validate the boundary-element predictions presented in these lecture notes were obtained by Mr. D. Stinebring (Applied Research Laboratory / The Pennsylvania State University, ARL/PSU).

The notional concepts presented herein, and the assessment of their status and potential value, represent the authors' opinions only; they do not in any way reflect the policies of the U.S. Government, the Department of Defense, the U.S. Navy, ONR, DARPA, NUWC, or any sponsoring or subsidiary organization.

REFERENCES AND BIBLIOGRAPHY

- Aris, R., (1962) *Vectors, Tensors, and the Basic Equations of Fluid Mechanics*, Prentice-Hall, Englewood Cliffs, NJ.
- Ashley, H., and M. Landahl (1965) *Aerodynamics of Wings and Bodies*, Dover, New York, NY.
- Birkgof, G., and E. Sarantonello (1957), *Jets, Wakes, and Cavities*, Academic Press, New York.
- Brennen, C.A. (1969), "Numerical Solution for Axisymmetric Cavity Flows," *J. Fluid Mech.*, 37.
- Brodetsky, S., (1923) "Discontinuous Fluid Motion past Circular and Elliptic Cylinders," *Proceedings of the Royal Society A102* (as summarized in May, 1975).

- Chou, Y.S., (1974) "Axisymmetric Cavity Flows past Slender Bodies of Revolution," *J Hydronautics*, 8(1).
- Dieval, L., C. Pellone, and M. Arnaud (2000) "Advantages and Disadvantages of Different Techniques of Modeling of Supercavitation," in LEGI (2000).
- Etkin, B., (1972) *Dynamics of Atmospheric Flight*, John Wiley & Sons, New York, NY.
- Fedorov, Y.A. (1960), "Motion of Wedge with Cheekbones Under Free Surface in Ideal Weightless Fluid," Tr. TzAGI. (In Russian.)
- Fine, N.E., (1992) *Nonlinear Analysis of Cavitating Propellers in Non-Uniform Flow*, PhD thesis, Massachusetts Institute of Technology, Cambridge, MA.
- Fine, N.E., and S.A. Kinnas, (1993) "A Boundary Element Method for the Analysis of the Flow Around 3-D Cavitating Hydrofoils," *J. Ship Research*, 37(1).
- Garabedian, P.R., (1956) "Calculation of Axially Symmetric Cavities and Jets," *Pacific J. of Math.* 6 (as summarized in May, 1975).
- Gieseke, T.J., editor, (1997) *Proceedings of the Third International Symposium on Performance Enhancement for Marine Applications*, Naval Undersea Warfare Center Division, Newport, RI.
- Greenwood, D.T., (1965) *Principles of Dynamics*, Prentice-Hall, Englewood Cliffs, NJ.
- Gregory, I.M., and R. Chowdhry (1994) "Hypersonic Vehicle Model and Control Law Development Using H_∞ and μ Synthesis," NASA TM 4562, National Aeronautics and Space Administration, Washington, DC.
- Kiceniuk, T., (1954) "An Experimental Study of the Hydrodynamic Forces Acting on a Family of Cavity-Producing Conical Bodies of Revolution Inclined to the Flow," CIT Hydrodynamics Report E-12.17, California Institute of Technology, Pasadena, CA (as summarized in May, 1975).
- Kirschner, I.N., D.C. Kring, A.W. Stokes, N.E. Fine, and J.S. Uhlman (2001) "Control Strategies For Supercavitating Vehicles," *J Vibration and Control*, accepted for publication.
- Kirschner, I.N., J.S. Uhlman, Jr., A.N. Varghese, and I.M. Kuria (1995) "Supercavitating Projectiles in Axisymmetric Subsonic Liquid Flows," *Proceedings of the ASME & JSME Fluids Engineering Annual Conference & Exhibition, Cavitation and Multiphase Flow Forum, FED 210*, J. Katz and Y. Matsumoto, editors, American Society of Mechanical Engineers, New York, NY.
- Kramer, F.S., (1998) "Multivariable Autopilot Design and Implementation for Tactical Missiles," *Proceedings of the 1998 AIAA Missile Sciences Conference*, American Institute of Aeronautics and Astronautics, Reston, VA.
- Kring, D.C., N.E. Fine, J.S. Uhlman, and I.N. Kirschner (2000) "A Time-Domain Cavitation Model using a Three-Dimensional Boundary-Element Method," submitted for a publication in honor of Prof. Y.N. Savchenko, Institute of Hydromechanics, Kiev, Ukraine.
- Kring, D.C., T. Korsmeyer, J. Singer, D. Danmeier, and J. White (1999) "Accelerated, Nonlinear Wave Simulations for Large Structures," *Proceedings of the 7'th Int'l Conference on Numerical Ship Hydrodynamics*, Nantes, France.
- Kuethe, A.M., and C-Y. Chow (1976) *Foundations of Aerodynamics: Bases of Aerodynamic Design*, Wiley, New York, NY.
- Lamb, H., (1945) *Hydrodynamics*, Dover, New York, NY.
- LEGI (2000) *Proceedings of the Scientific Meeting on High-Speed Hydromechanics and Supercavitation*, Laboratoire des Ecoulements Géophysiques et Industriels, Grenoble, France.
- Logvinovich, G.V. (1969), *Hydrodynamics of Flows with Free Boundaries*, Naukova Dumka, Kiev. (In Russian.)
- Logvinovich, G.V., (1980) "Some Problems in Planing Surfaces [sic]," translated from "Nekotoryyi voprosy glissirovaniya i kavitatsii [Some Problems in Planing and Cavitation]," *Trudy TsAGI 2052*, Moscow, Russia.
- Logvinovich, G.V., V.N. Buivol, A.S. Dudko, S.I. Putilin, and Y.R. Shevchuk (1985) *Flows with Free Surfaces*, Naukova Dumka, Kiev, Ukraine (in Russian).
- Maniar, H.D., (1995) *A Three-Dimensional Higher-Order Panel Method Based on B-Splines*, PhD thesis, Massachusetts Institute of Technology, Cambridge, MA.

- MATH WORKS (1998) Control System Toolbox for Use with MATLAB®, The Math Works, Inc., Natick, MA.
- May, A., (1975) “Water Entry and the Cavity-Running Behavior of Missiles,” SEAHAC TR 75-2, Naval Sea Systems Command, Arlington, VA.
- Michel, J.M., “Overview of Former Researches on Supercavitation Carried Out at LEGI/IMG [sic],” in LEGI (2000).
- Münzer, H., and H. Reichardt, (1950) “Rotational Symmetric Source-Sink Bodies with Predominantly Constant Pressure Distributions [sic],” ARE Translation 1/50, Aerospace Research Establishment, England, (as summarized in May, 1975).
- Newman, J.N., (1980) Marine Hydrodynamics, MIT Press, Cambridge, MA.
- Phillips, J.R., and J. White (1997) “A Precorrected-FFT Method for Electrostatic Analysis of Complicated 3D Structures,” IEEE Trans. on Computer-Aided Design, 16(10).
- Plesset, M.S., and P.A. Shaffer (1948), “Cavity Drag in Two and Three Dimensions,” J. Appl. Phys. 19.
- Raven, F.H., (1961) Automatic Control Engineering, McGraw-Hill Book Company, New York, NY.
- Reichardt, H., (1946) “The Laws of Cavitation Bubbles at Axially Symmetrical Bodies in a Flow [sic],” Ministry of Aircraft Production Volkenrode, MAP-VG, Reports and Translations 766, Office of Naval Research, Arlington, VA, (as summarized in May, 1975).
- Romanovsky, B.I., Y.A. Fedorov, and Z.I. Kramina (1970), “Calculation of Hydrodynamic Characteristics of Wedges in a Boundless, Weightless Fluid,” Tr. TzAGI. (In Russian.)
- Savchenko, Y.N., V.N. Semenenko, and V.V. Serebryakov (1992), “Experimental Research into Supercavitating Flows at Subsonic Speeds,” Doklady AN Ukranini. (In Russian.)
- Savchenko, Y.N., (2000) “Supercavitation: Applications and Perspectives,” in LEGI (2000).
- Savchenko, Y.N., V.N. Semenenko, Y.I. Naumova, A.N. Varghese, J.S. Uhlman, and I.N. Kirschner (1997) “Hydrodynamic Characteristics of Polygonal Contours in Supercavitating Flow,” in Gieseke (1997).
- Schlichting, H., (1979) Boundary-Layer Theory, McGraw-Hill, New York, NY. Translated by J. Kestin.
- Semenenko, V.N., (2000) “Dynamics of Supercavitating Bodies,” in LEGI (2000).
- Stokes, A.W., and D.C. Kring (2000) ETC_Supercav, underwater flight simulation software package, Engineering Technology Center, Mystic, CT.
- Tulin, M.P., (1958) “New Developments in the Theory of Supercavitating Flows,” Proceedings of the Second Symposium on Naval Hydrodynamics, Office of Naval Research, Arlington, VA, (as summarized in May, 1975).
- Tulin, M.P., (1959) “Supercavitating Flow Past Slender Delta Wings,” J Ship Research, 3(3).
- Tulin, M.P., (1964) “Supercavitating Flows – Small Perturbation Theory,” J Ship Research.
- Uhlman, J.S., (1987), “The Surface Singularity Method Applied to Partially Cavitating Hydrofoils”, Journal of Ship Research, 31(2).
- Uhlman, J.S., (1989), “The Surface Singularity or Boundary Element Method Applied to Supercavitating Hydrofoils”, Journal of Ship Research, 33(1).
- Uhlman, J.S., A.N. Varghese, and I.N. Kirschner (1998) “Boundary-Element Modeling of Axisymmetric Supercavitating Bodies,” Proceedings of the 1st HHTC CFD Conference, Naval Surface Warfare Center Carderock Division, Carderock, MD.
- Vada, T., and D.E. Nakos (1993) “Time-Marching Schemes for Ship Motion Simulations,” 8th Int’l Workshop on Water Waves and Floating Bodies.
- Varghese, A.N., J.S. Uhlman, Jr., and I.N. Kirschner (1997) “Axisymmetric Slender-Body Analysis of Supercavitating High-Speed Bodies in Subsonic Flow,” in Gieseke (1997).
- Waid, R.L., (1957) “Cavity Shapes for Circular Disks at Angles of Attack,” CIT Hydrodynamics Report E-73.4, California Institute of Technology, Pasadena, CA (as summarized in May, 1975).
- Wang, Q., and R.F. Stengel (1998) “Robust Control of Nonlinear Systems with Parametric Uncertainty,” Proceedings of the 37th IEEE Conference on Decision and Control, Institute of Electrical and Electronics Engineers, Inc., New York, NY.
- Wu, T.Y-T, “A Free Streamline Theory for Two-Dimensional Fully Cavitated Hydrofoils [sic],” Journal of Mathematics and Physics 35 (as summarized in May, 1975).
- Yih, C-S., (1979) Fluid Mechanics, West River Press, Ann Arbor, MI.

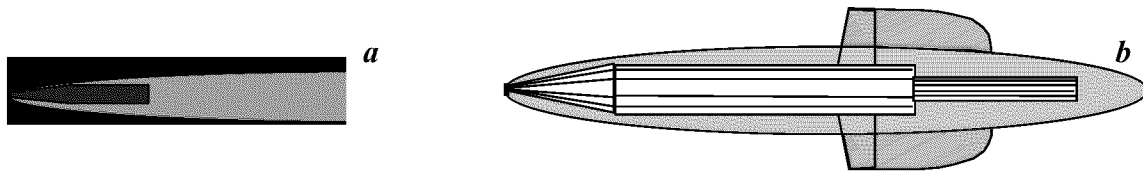


Figure 1. Two classes of supercavitating high-speed bodies: (a) Free-flying projectiles; (b) Self-propelled vehicles



Figure 2. Free-Body Diagram for Undersea Vehicle Drag Analysis

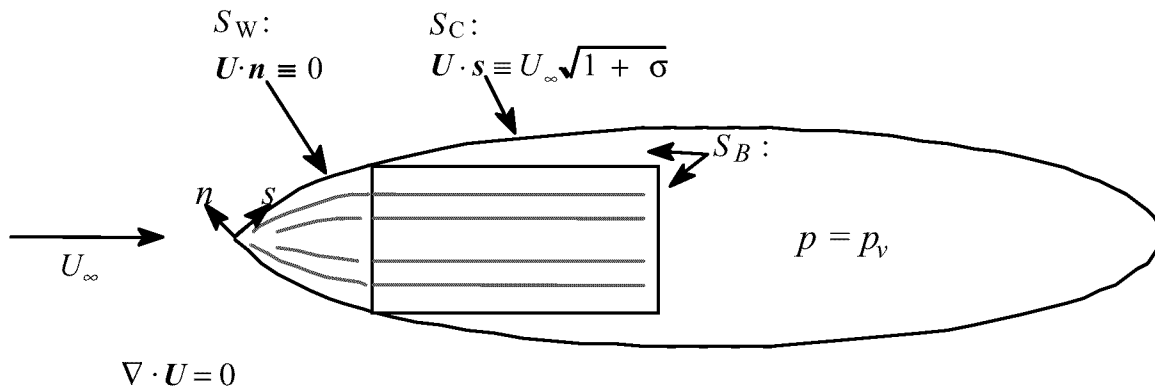
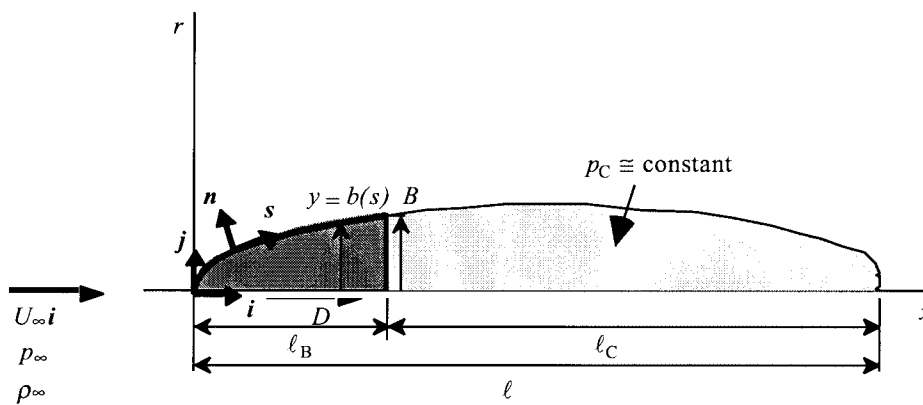


Figure 3. A Boundary-Value Problem for Ideal Supercavitating Flow.



5.5...1.1.1.1

Figure 4. Physics problem for axisymmetric supercavitating flow.

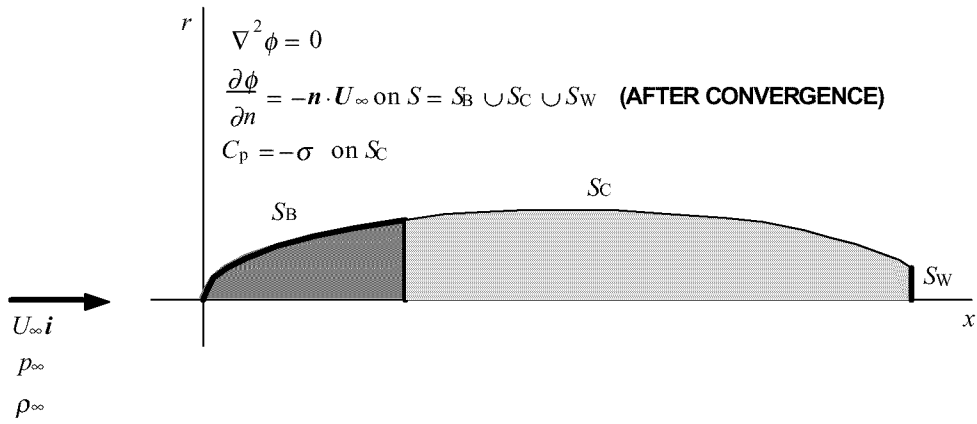


Figure 5. Boundary-value problem for axisymmetric supercavitating flow.

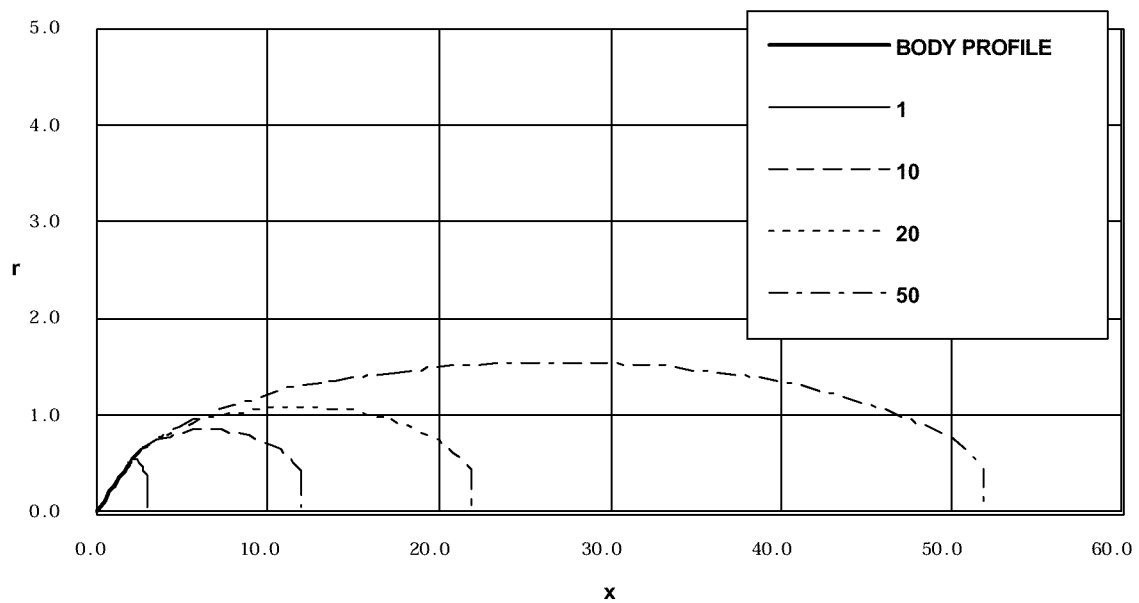


Figure 6. Body-cavity profiles for a 15° cone for dimensionless cavity lengths shown (scaled for viewing). The corresponding predicted cavitation numbers (decreasing with length) are 0.501, 0.070, 0.038, and 0.017

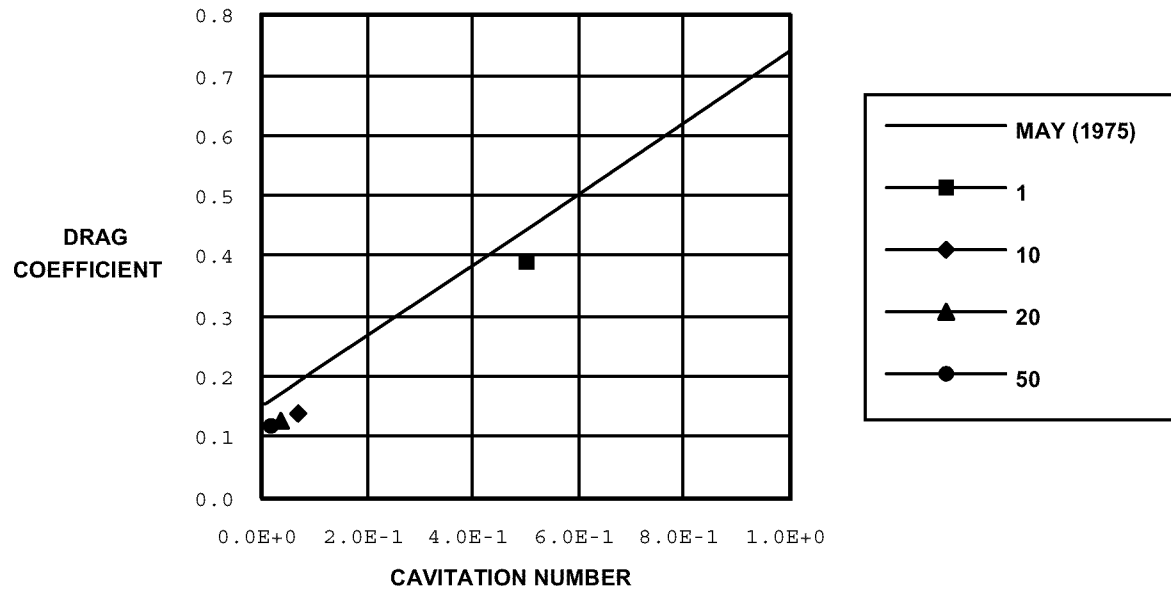


Figure 7. Predicted drag coefficients versus cavitation number for a 15° cone at dimensionless cavity lengths shown. The empirical curve fit of May (1975) is based on results of experiments by various researchers.

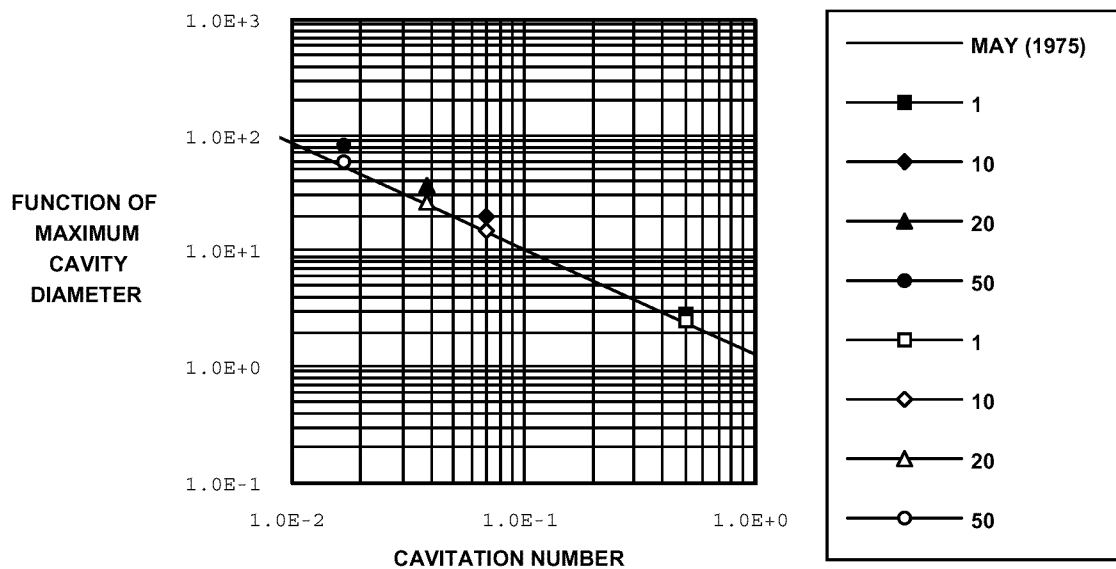


Figure 8. Predicted cavity diameter versus cavitation number for a 15° cone at dimensionless cavity lengths shown. The empirical fit of May (1975) is based on results of experiments by various researchers. Solid markers are based on the computed drag coefficient; open markers are based on the drag coefficient given by the empirical curve fit of May (1975). The function of diameter is given in the text at equation 3.18.

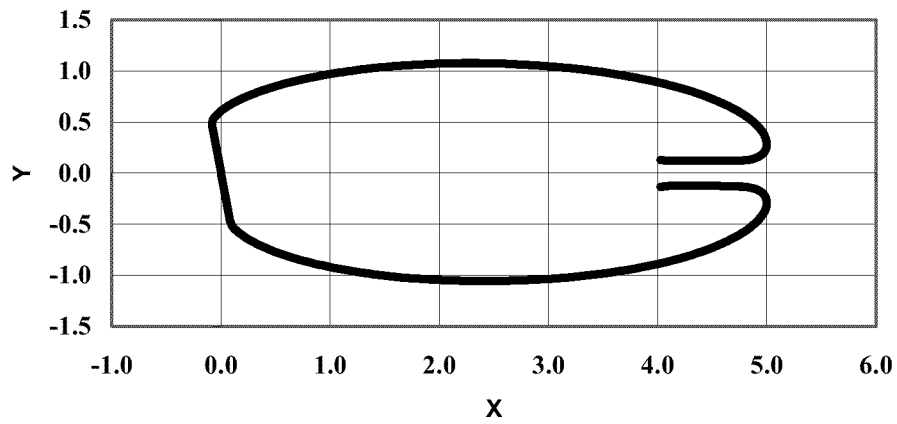


Figure 9. 2D cavity shape for a flat plate cavitator with $l/d = 5.0$ and $\alpha = 10^\circ$.

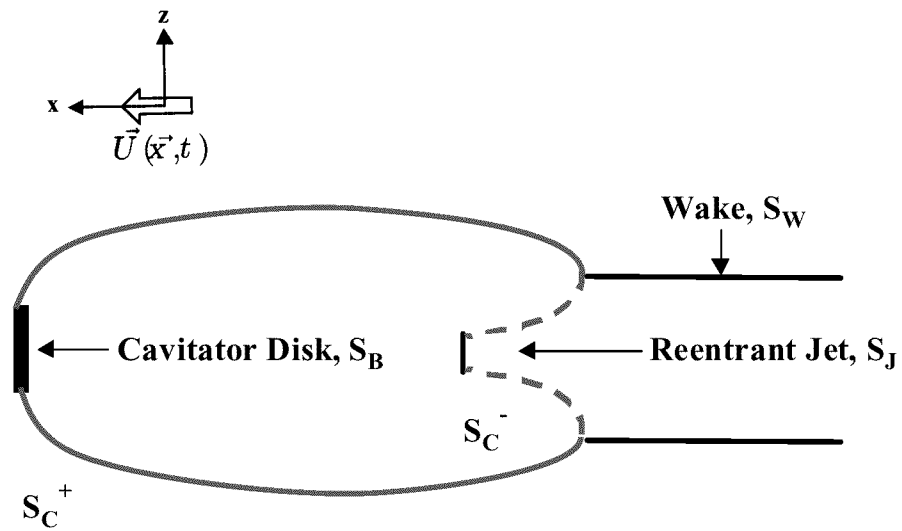


Figure 10. The initial boundary-value problem for unsteady boundary element simulations.

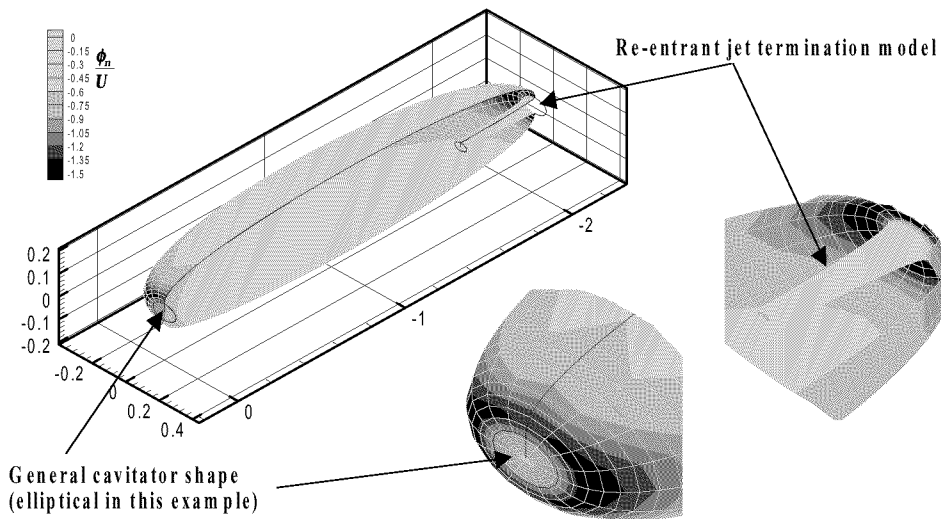


Figure 11. Normal velocity at start-up, with a homogenous initial condition for the cavity potential and an assumed initial geometry.

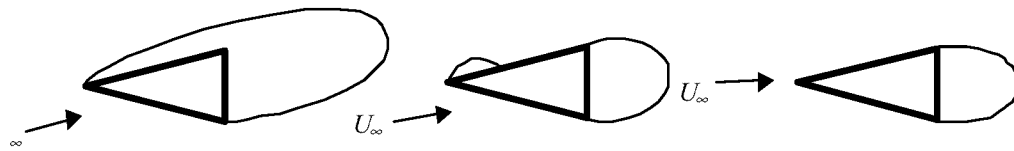


Figure 12. The three regimes of cavitating wedges, fully-, partially- and base cavitating.

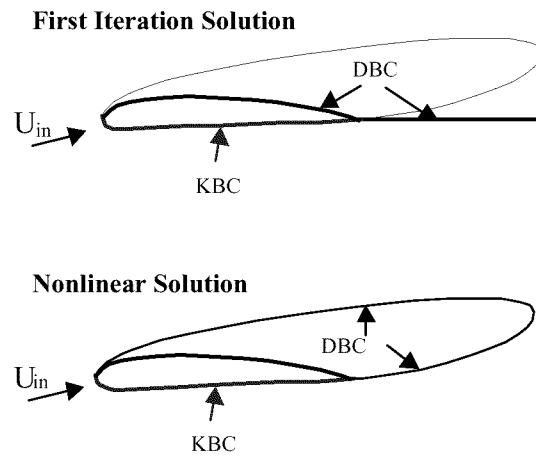


Figure 13. Sketch demonstrating the difference between the first iteration and nonlinear solutions. LScav solves for the first iteration solution.

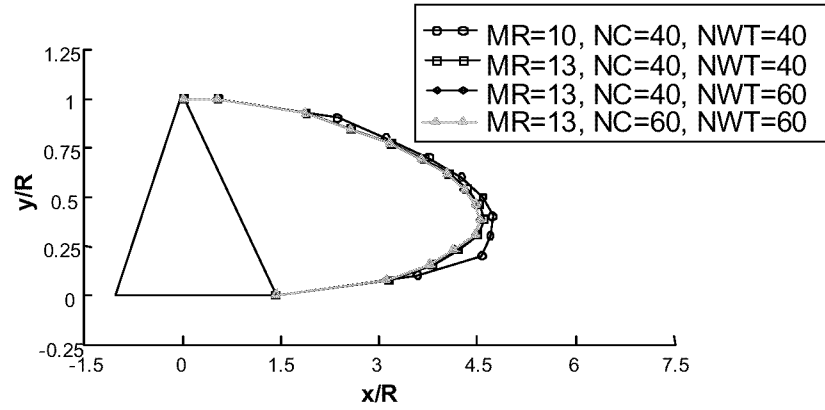


Figure 14. Convergence of cavity planform a fin with 45° sweepback and 7.5° wedge angle (note: the plot is not drawn to scale).

Table 1. Sample LScav results showing convergence of cavity volume, lift, and drag coefficients with number of panels

# Panels	Volume	C_L	C_D
800	1.218	.1032	.0174
1040	1.129	.1024	.0174
1300	1.106	.1031	.0174
1560	1.104	.1036	.0175

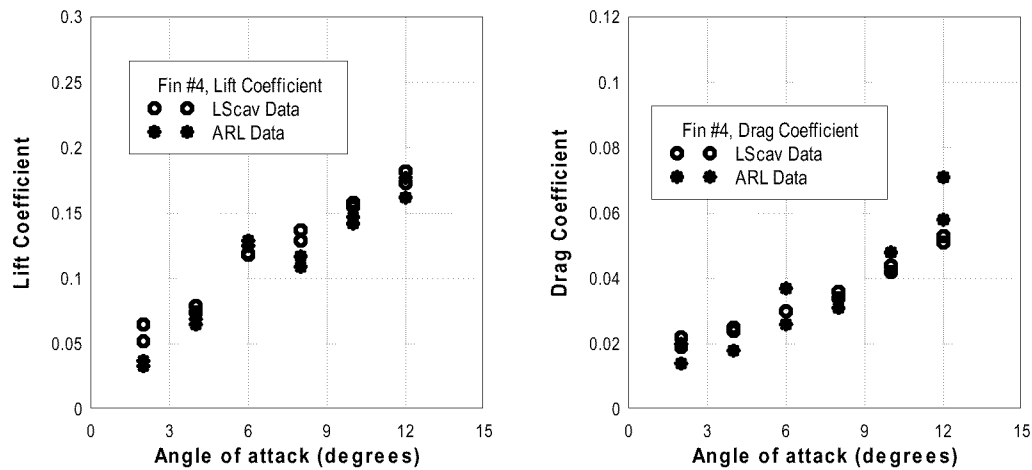


Figure 15. Comparison of measured and computed lift and drag coefficients (measured data provided by D. Stinebring, ARL/PSU)

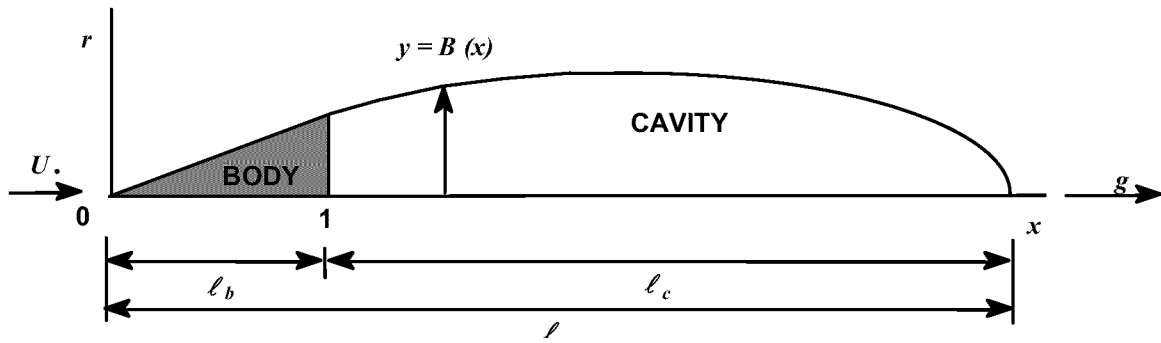


Figure 16. Physical problem addressed by slender body theory.

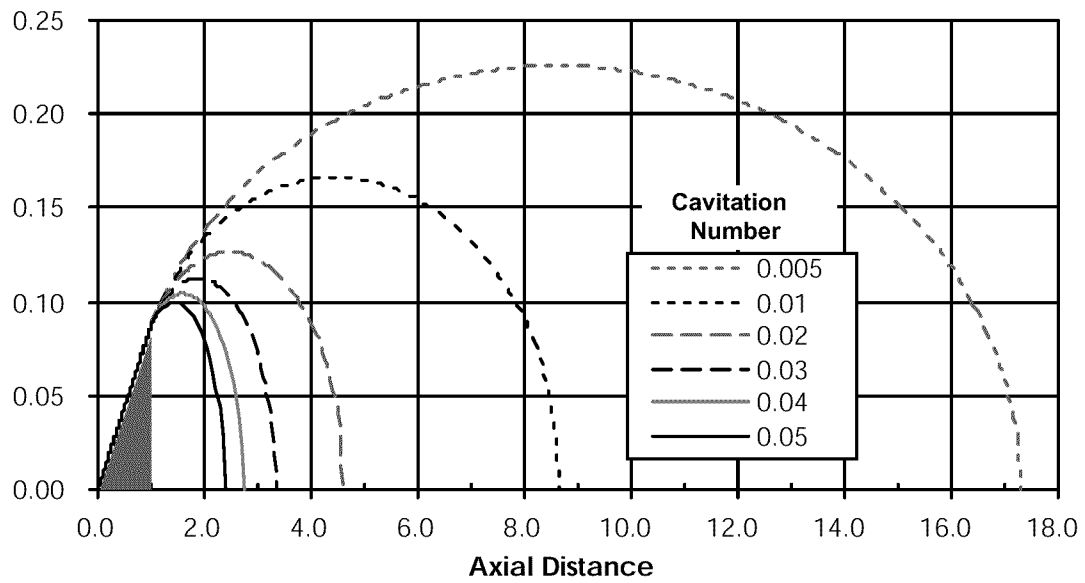


Figure 17. Cavity shapes for different cavitation numbers for axisymmetric supercavitating flow past a 10° cone in an incompressible fluid.

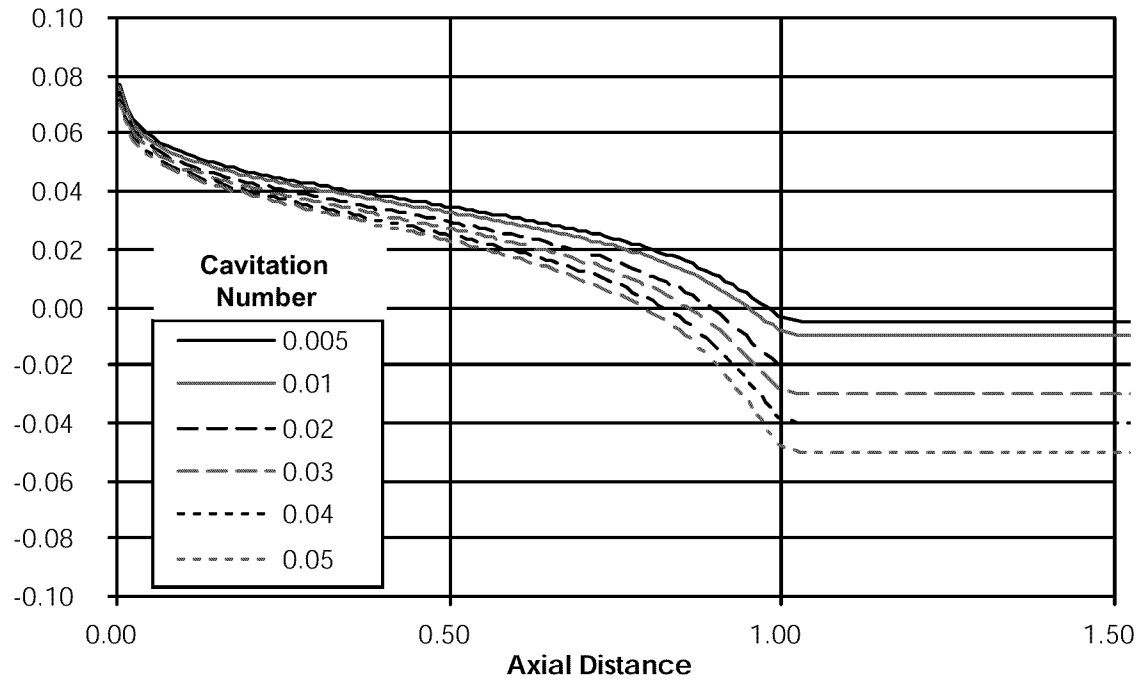


Figure 18. Predicted Surface Pressure Distributions for Various Cavitation Numbers for Axisymmetric Supercavitating Flow Past a 10° Cone in an Incompressible Fluid

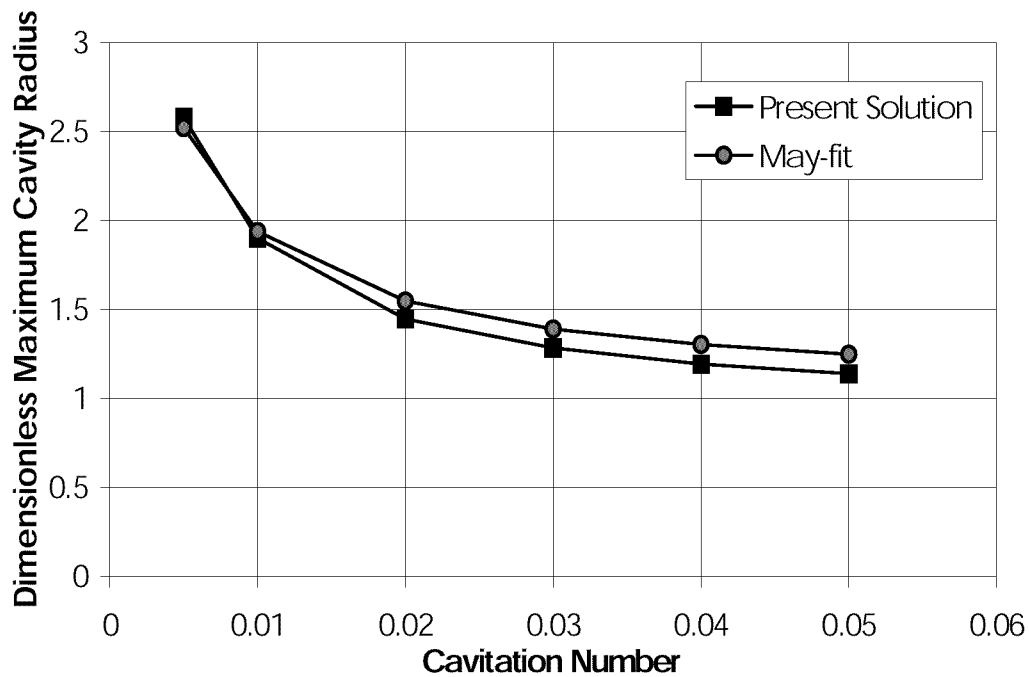


Figure 19. Cavity Maximum Radius Versus Cavitation Number for Axisymmetric Supercavitating Flow Past a 10° Cone in an Incompressible Fluid

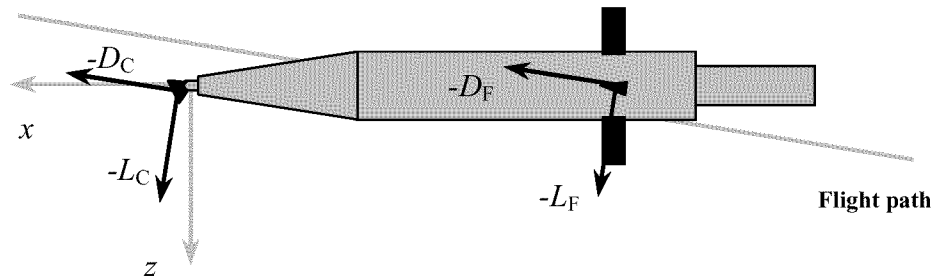


Figure 20. Nomenclature

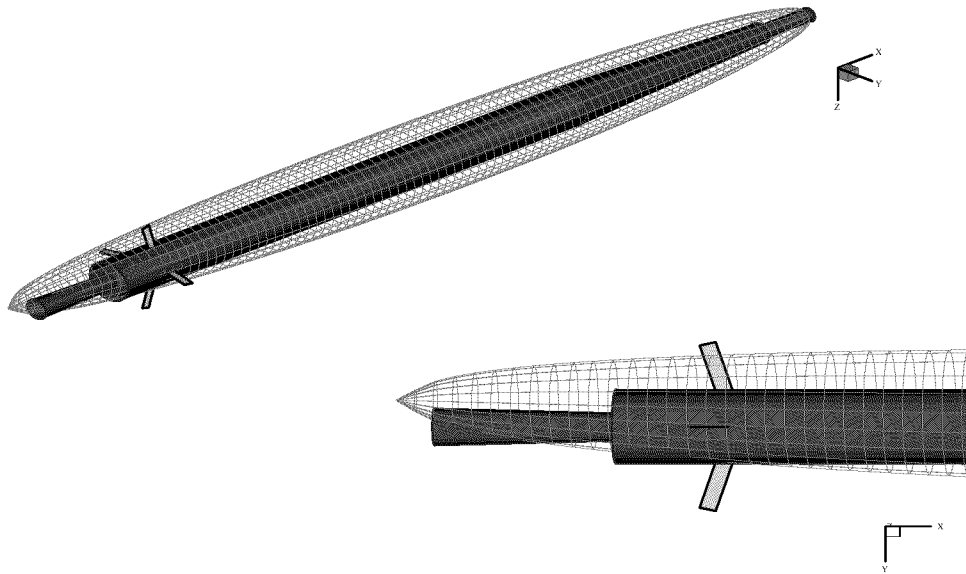


Figure 21. Cavity behavior in an extreme turn

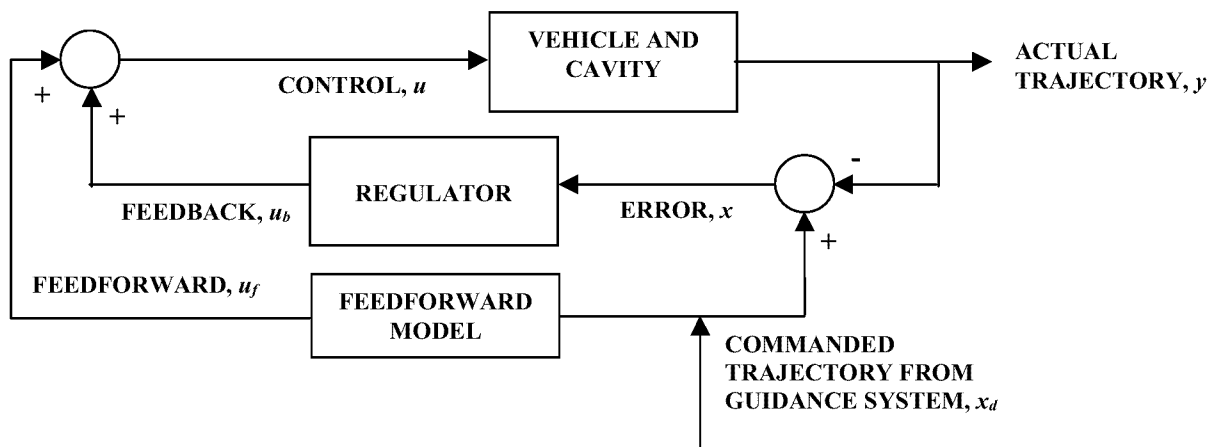


Figure 22. Simplified dynamical systems model of a supercavitating vehicle.

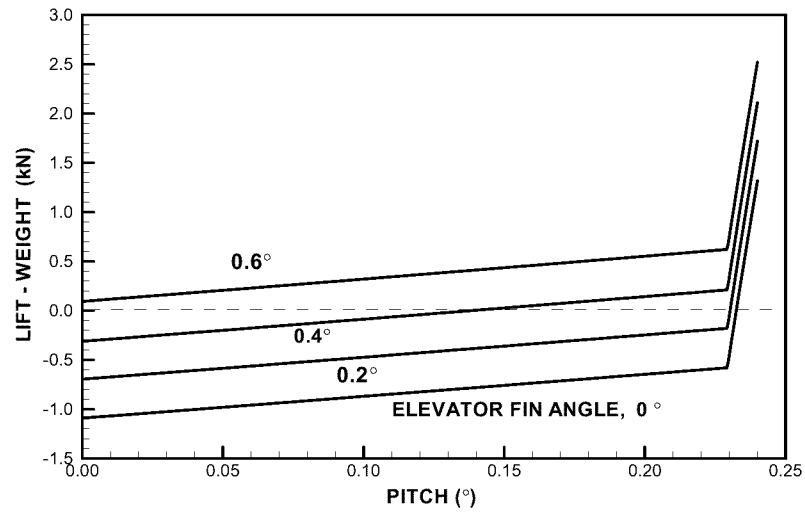


Figure 23. Lift margin as a function of pitch and elevator angles.

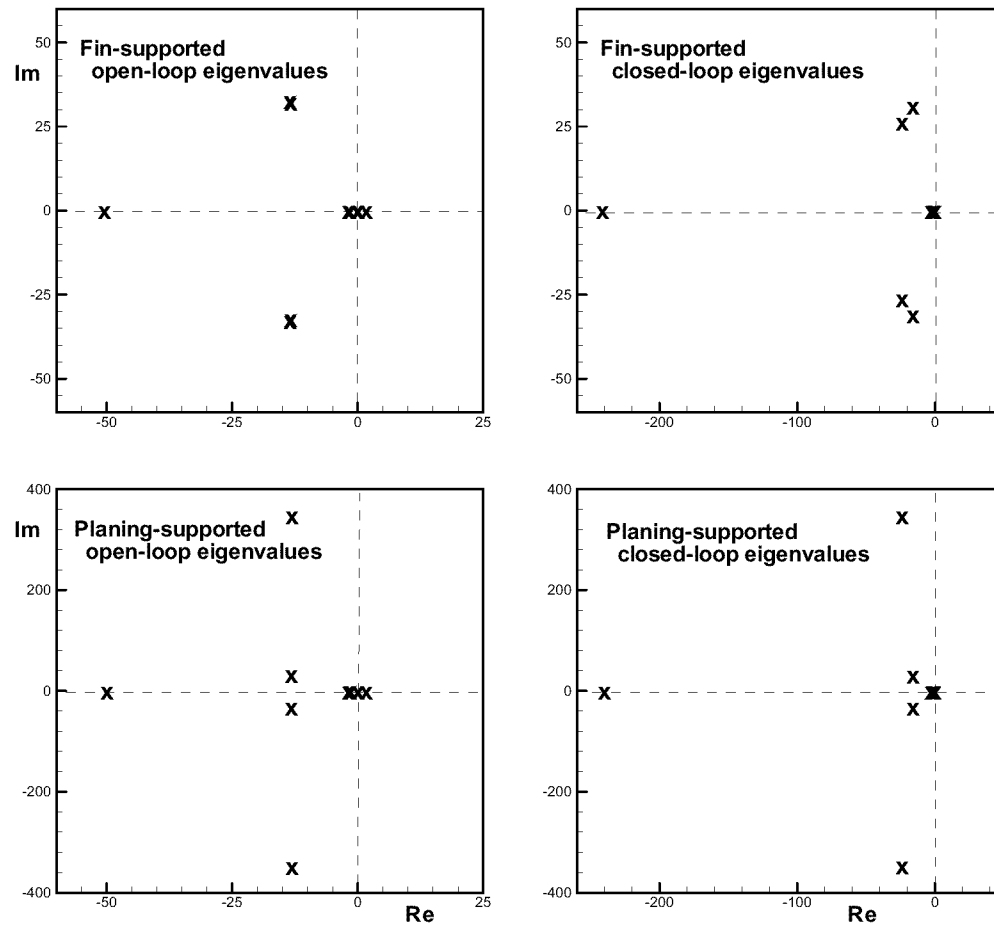
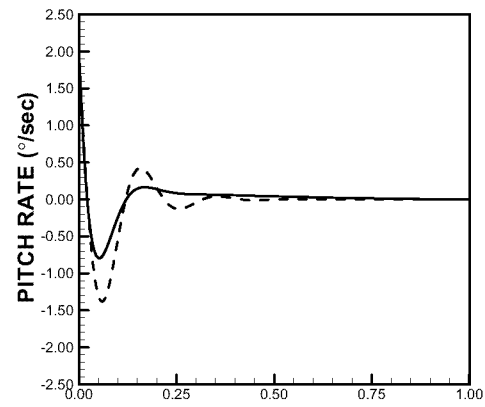
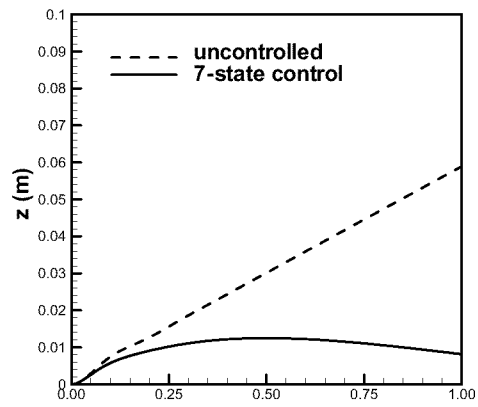


Figure 24. Open- and closed-loop eigenvalues for two modes of afterbody support.

Initial Perturbation in Pitch Rate = 1 °/sec



Initial Perturbation in Pitch Rate = 20 °/sec

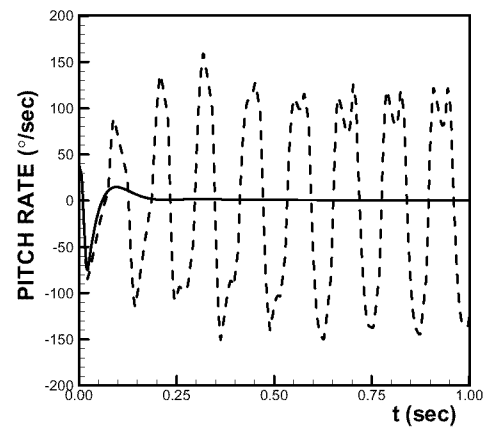
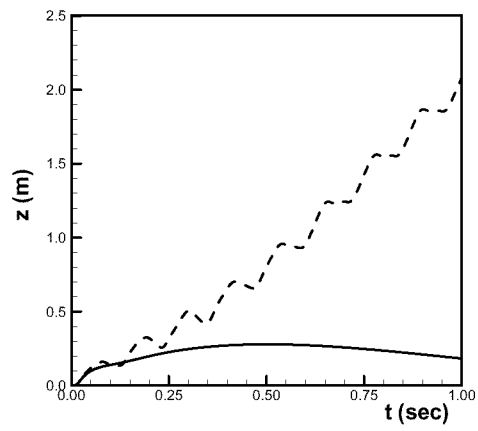


Figure 25. *Fin-supported straight and level flight with small and large perturbations.*

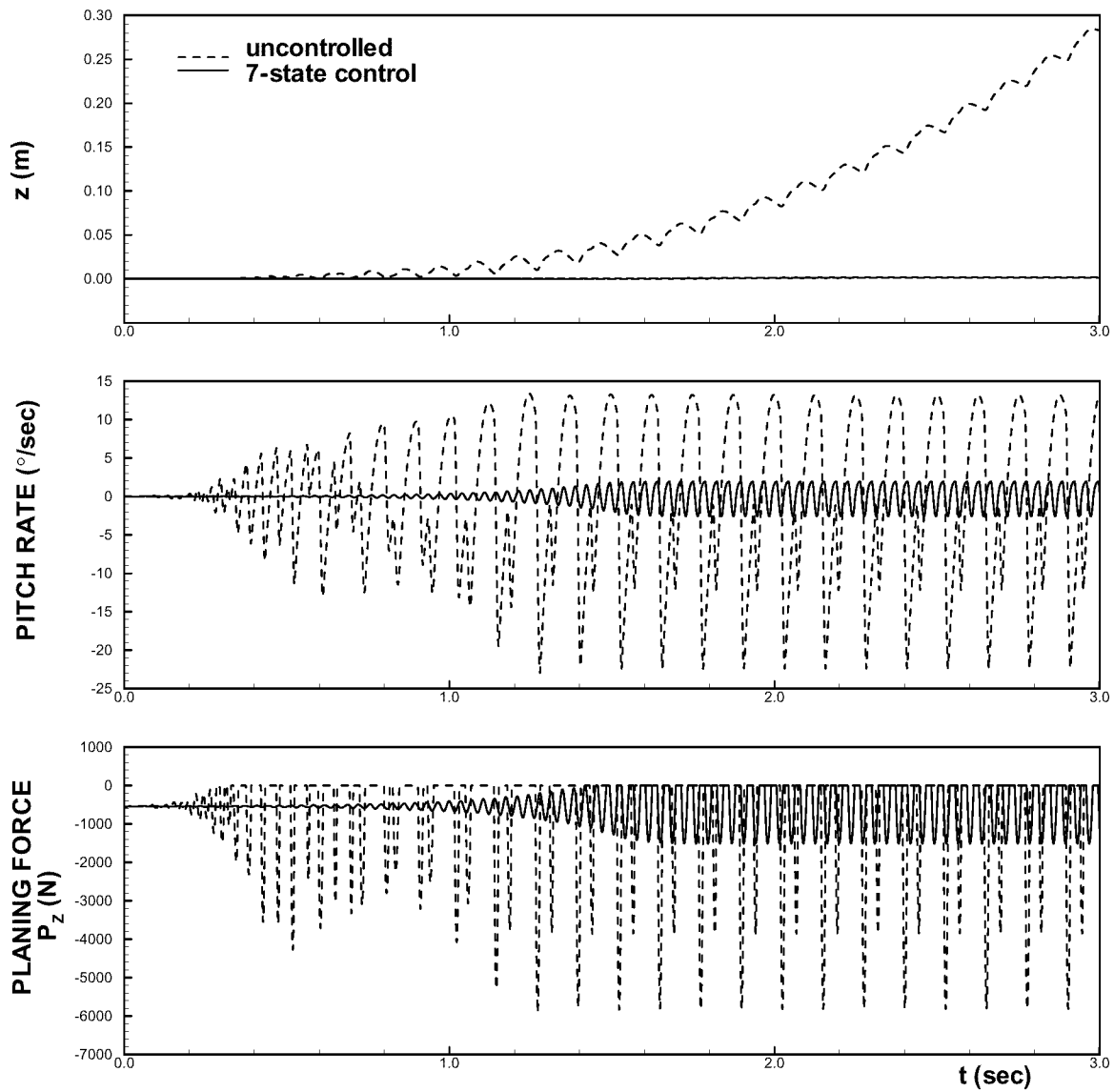


Figure 26. Planing-supported straight and level flight with an initial pitch rate perturbation of 0.01%/s with 7-state control.